UNIVERSITY OF SOUTHAMPTON

FACULTY OF PHYSICAL AND APPLIED SCIENCES

Optoelectronics Research Centre

Statistical description of high-harmonic generation

by

Arthur Degen-Knifton

Thesis for the degree of Master of Philosophy

UNIVERSITY OF SOUTHAMPTON

ABSTRACT

FACULTY OF PHYSICAL AND APPLIED SCIENCES
Optoelectronics Research Centre

Master of Philosophy

STATISTICAL DESCRIPTION OF HIGH-HARMONIC GENERATION

by Arthur Degen-Knifton

Here, we present a novel method for estimation of harmonic spectrum features generated from ultrashort high-intensity laser pulses propagating through gas-filled capillaries, based on pump pulse decomposition and statistical considerations.

Because of the strong optical nonlinearity, a high-intensity pump pulse launched with a simple, e.g. Gaussian, temporal profile develops a highly complex structure during propagation. We show how such complex propagating ultrashort infrared pulses can be decomposed and subdivided to provide more in-depth analysis of each of their intense regions, leading to a complete diagnostic view of the relevant features of ultrashort pulses for nonlinear optics, e.g. the number, peak intensities, and temporal widths of these individual pulse components within the complex structure. This analysis provides more insight into the collective action of all pulse components as opposed to traditional means which focus on a single feature, and allows diagnosis of the evolution of the large ensemble of features found in such intense ultrashort pulses.

This analysis is then used to inform an approximation of the high harmonic spectrum generated from such a pulse based on the cumulative harmonic generation of each of the propagating pulse components. We show that this method is $\sim$57 times faster than explicit simulation, requires significantly less computational power, and provides good approximations to many features of the generated high harmonic spectra. We see that this method provides a strong complementary approach to finding optimal conditions for generating the highest harmonics, and provides an intuitive system for identifying the root of certain harmonic pulse features and potentially for predicting the conditions for generating them.

Contents

List of Figures

Declaration of Authorship

I, Arthur Degen-Knifton, declare that the thesis entitled *Statistical description of high-harmonic generation* and the work presented in the thesis are both my own, and have been generated by me as the result of my own original research. I confirm that:

- this work was done wholly or mainly while in candidature for a research degree at this University;
- where any part of this thesis has previously been submitted for a degree or any other qualification at this University or any other institution, this has been clearly stated;
- where I have consulted the published work of others, this is always clearly attributed;
- where I have quoted from the work of others, the source is always given. With the exception of such quotations, this thesis is entirely my own work;
- I have acknowledged all main sources of help;
- where the thesis is based on work done by myself jointly with others, I have made clear exactly what was done by others and what I have contributed myself;
- parts of this work have been published as:

  - Statistical description of capillary-based high-harmonic generation *CLEO EU, Munich, Germany 21-25 Jun 2015*

  - Statistical analysis of pump-pulse propagation in gas-filled capillaries for high-harmonic generation *Photon 14 - IoP 1-4 Sep 2014*

Signed:.....

Date:.....

Acknowledgements

Thanks to my friends and family for their support and to my supervisors for making this possible.

Chapter 1

Introduction

Since the advent of laser technology in 1960 [3], lasers of increasingly high intensity have become widely available [4][5], driving significant interest in the nonlinear responses they elicit in optical materials [6][7][8]. Despite the rapid development of high intensity lasers and their uses in nonlinear optics, the field has been constrained by the availability of short (<100 nm) wavelength lasers [9] which are required for a large variety of both scientific and industrial applications. A particularly interesting short wavelength regime is the extreme ultraviolet (XUV) (10-120 nm), at the length scale of many artificial and biological structures [10] which are difficult to image by other means; unfortunately, to this day, the main sources of XUV radiation are expensive and bulky (see section 1.2). There is one laser source, however, which allows for relatively inexpensive tabletop XUV generation, known as High-Harmonic Generation (HHG), which has grown in popularity and utility since it was first shown in gases in 1987 [11].

HHG relies on the nonlinear response of a solid or gas to an intense pump laser in order to coherently generate harmonics of the laser, at odd multiples of the laser frequency. These harmonics can persist far into the XUV and soft x-ray (0.1-10 nm) regime and with a sufficiently bright pump can themselves have high flux. The main problem with this method of XUV generation is that the highly nonlinear nature of the process results in highly localized generation around the laser focus, and hence relatively little XUV is generated given the laser powers required and the effective conversion efficiency between near-infrared (NIR) and XUV is relatively low.

The difficulties of short interaction lengths in HHG can be compensated for by the use of a waveguide to contain the pump pulse and maintain intensity and hence XUV generation over several centimetres. To this end, capillary-based HHG [12] uses a capillary waveguide to maintain pump pulse intensity over a distance of several cm, and hence produces significant XUV flux at the capillary output. A major drawback of this method for HHG is that it makes modelling significantly more difficult and hence most of the progress in this area has been experimentally driven.

The primary goal of this project is to develop the capillary-based HHG system to produce more XUV flux in the 20-40 nm regime and expand upon the optimisations of recent papers [2][13]. This will be performed primarily through numerical modelling and simulation, building upon models developed previously by the group [2], with the intention to provide a framework for easily predicting HHG spectrum features based on pump laser properties, in support of the imaging work being done within the group [14].

1.1 Applications of ultrashort and XUV optical pulses

Generating coherent XUV, despite the difficulties involved, is very important for a range of applications. Given that generating short wavelength coherent radiation below the XUV range is extremely difficult, XUV is required to fulfil many nanoscale imaging [14][15] and femto- and attosecond applications [16] [17].

Nanoscale imaging utilises short optical wavelengths to image objects of nanometre scale. Given that the wavelengths of XUV/soft x-ray are typically smaller than details of nanoscale objects, these wavelengths can be used to image such nanoscale objects. The high flux and wide bandwidth offered by the HHG system allows for imaging of many nanoscale objects quickly without risk of insufficiently high flux of the shortest wavelengths. This provides stark advantages over traditional methods of non-optical nanoscale imaging, such as atomic-force microscopy (AFM) [18] and electron-based methods, such as transmission electron microscopy (TEM) [19], and scanning electron microscopy (SEM) [20]. AFM produces atomic-scale resolution images of a surface but since it requires scanning line by line over the surface, such images can be relatively slow to obtain this way, and the surface must also be relatively flat and have smooth depth changes compared to the scale of the scanning tip ($\sim \mu$m) or a huge loss of resolution will result [21]. The electron-based imaging methods do provide some benefit over AFM, despite not achieving AFM's atomic scale resolution. The biggest benefits are the faster imaging times, given that electron beams can be scanned quickly across a sample and can resolve a characteristically large depth of field, although for all these benefits, electron-based imaging methods require specific sample conditions to produce high resolution images. Many objects must be stained or dried to increase their electron optical contrast to allow for resolution of separate structures within an object. TEM has the specific requirement of ultrathin samples, since the electron beam must be detectable after passing through the sample; this disallows many objects from being imaged this way, although many objects can be cut to this thickness. SEM also has a similarly restrictive condition in that any imaged surfaces must be conductive to be easily imaged, and to this end many non-conductive objects like biological samples must be metal coated before imaging, which may damage the sample or obscure fine details in the surface [22].

The alternative methods of nanoscale imaging include sub-diffraction methods, which allow for nanoscale imaging with long wavelength lasers. These methods include interferometric [23] and 4PI [24] methods, although these also have their own disadvantages, for example, interferometric imaging is entirely dependent on having very high coherence of the light source and extremely high quality optics to produce clean images, while 4PI imaging requires that samples fluoresce during illumination by the laser. The other main method of achieving sub-wavelength imaging resolution is the use of near-field imaging [25] systems, which employ components smaller than the optical wavelength used, and hence use evanescent fields to image surfaces, although such surfaces must have a sub-wavelength separation from the imaging device and such devices intrinsically require extremely high precision fabrication to maintain high resolution.

With so many limitations on imaging speed and resolution, a compact, bright, coherent source of XUV such as capillary-based HHG has the potential to provide significant advantages over current imaging methods, since it allows for simple, direct imaging.

The other main application of XUV is the generation of attosecond pulses, most commonly used in studies of femto- and attosecond scale dynamics, such as atomic and electronic dynamics [26], which require pulses with length much shorter than the time scale of the dynamics being imaged. Such attosecond pulses are generated by gating the isolated HHG pulses that result from the broadband HHG spectrum, usually by polarization gating or a second pump wavelength [27].

1.2 Current XUV sources

The most prodigious source of coherent XUV, synchrotrons were the only source until the advent of free electron lasers and HHG. Even now they have enormous power and space demands and can easily cost $>$ £100 million to build. They consist of evacuated tubes forming N-sided polygons with bending magnets at each corner. Relativistic electrons are accelerated around the synchrotron and at each corner they radiate tangentially as they are bent. This radiation can then be collected and filtered to produce the desired light source. Due to the nature of the machine the radiation is relatively short pulse, $\sim$ picosecond full width half maximum (FWHM), which is very long compared to the $\sim$ femtosecond pulse FWHMs available from HHG sources, although it is partially compensated for by the wide potential wavelength ranges (between 0.5Å and 1μm for the Diamond Light Source [28]).

Free electron lasers (FELs) operate on very similar principles to synchrotrons, except they use accelerated electrons, usually from a linear accelerator, which then pass through an undulator which consists of a series of alternating magnetic fields which cause the electrons to oscillate perpendicular to their propagation direction. This oscillation causes the electrons to radiate in the propagation direction. In a strong undulator, the electrons

bunch because of the sinusoidal ponderomotive force along the propagation path; this causes the electrons to emit their photons in phase and in very short bursts, resulting in ultrashort ($\sim$ fs [29]) coherent pulses with wavelengths between microwave and x-ray. Such pulses can have the ideal combination of high flux, ultrashort length, short wavelength, and strong coherence, although there are some distinct disadvantages to using FELs, especially at x-ray wavelengths.

Firstly, FELs, like synchrotrons, require a lot of space and power; a linear accelerator producing the desired electron energies to generate x-rays can be $>$ km in length and require large amounts of power to run, as well as requiring physical reconfiguration to change electron energies. Likewise, the undulator requires a lot of energy to run and cool, and because the oscillation frequency depends on the period of the undulator, it must be physically reconfigured to produce different wavelengths, which requires a lot of time and work. Because of this, many FELs have very limited wavelength ranges, such as LCLS at Standford which has a generating range of 4.5 nm - 1.3 Å [30]. Ignoring the enormous cost of building and running an FEL, it is still extremely impractical for most laboratories and groups who need a compact source with more tunability and lower running costs.

1.3 History of high-harmonic generation

The foundation for HHG was lain long before its inception with the 1960 invention of the laser [3] and the subsequent discovery of nonlinear optical responses [6]. The first actual HHG came in 1977, and used a high power CO_2 laser to generate harmonics from planar aluminium targets, although this level of laser intensity was not widely available until the invention of chirped pulse amplification (CPA) [31] and the Ti:Sapphire laser [5] in 1985 and 1986, respectively. With this new availability of high intensity laser sources, HHG was shown in gases a year later [11], and the development of HHG began.

Most early progress on HHG was experimental due to the difficulty of simulating and predicting the HHG spectrum given the lack of computing power at the time, however early attempts at explicit simulation [32] provided invaluable single-atom spectra and gave a first prediction of the cutoff harmonic frequency. Subsequent attempts at simulation [33] [34] [35] adopted a semi-classical approach which allowed for rapid simulation and gave rise to many theoretical predictions, particularly the cutoff law (eq 2.11) which allowed for rapid development of HHG sources.

The first use of a capillary waveguide in HHG came in 1998 [12] in an attempt to achieve longer laser-gas interaction lengths. Early theoretical development of the capillary HHG source came in 1999 with the first analysis of the nontrivial, but highly beneficial, phase-matching benefits of the capillary waveguide [36], using the capillary waveguiding theory

of [37]. This also gave rise to subsequent optimisation of capillary HHG sources in [38], providing a general set of capillary and parameters for effective HHG in capillaries.

Full simulation of capillary based HHG became viable with the publishing of nonlinear pulse propagation equations [39] for the pump pulses used, allowing for the development of better simulations [40] and standardised models of pump pulse propagation and semi-classical HHG [41] [17]. These improved and standardised models gave rise to studies of phase matching and pump pulse growth [42] [13] [2] which provided the capillary optimisations which are used today.

1.4 Project aims

The primary aim of this project is to provide a framework for predicting harmonic spectra based on initial system conditions in as time-efficient manner as possible, with the ultimate intention of optimizing the input pulse energy and the gas pressure to provide as bright harmonics in the 20-35 nm range as possible, while simultaneously using these findings and to learn more about the structure and processes in the pump pulse propagation and subsequent HHG, such as the combined phase-matching conditions produced by the non-trivial nonlinear interactions between gas, laser, and plasma.

1.5 Experimental Setup

The system being modelled in this thesis is the optimized capillary-based HHG system developed within the group, [2] [42] and [13], as seen in figure 1.1. This setup has been somewhat optimized in terms of length and much analysis has been done on it, making it an ideal baseline for further analysis and optimization. The dimensions of the system are as follows:

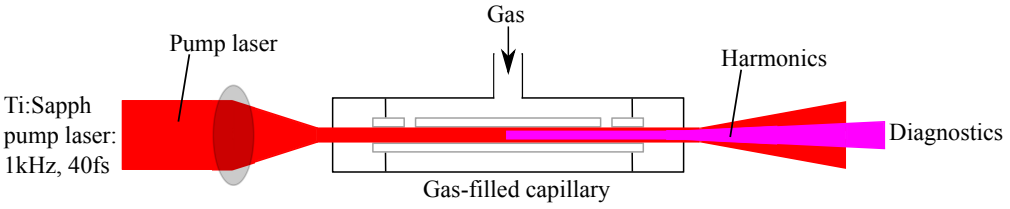

Figure 1.1: Schematic diagram of the experimental setup.

A 7 cm long, 75 μm radius, fused silica capillary, with gas holes drilled 3 and 5 mm from the front and back of the capillary waveguide, respectively. The capillary itself is filled with argon by pumping the region around the capillary midsection to the desired pressure. The region either end of the capillary is pumped down to high vacuum to stop the heavy absorption of any generated XUV by the neutral air and attenuation and nonlinear defocusing of the pump beam by ionized air near the focus.

The pump laser is a Ti:Sapphire system with a 1kHz repetition rate and an 800nm central wavelength. The pulse shape is Gaussian to a good approximation with approximately 40fs full-width-half-maximum (FWHM). This beam is focused by a 600 mm focus lens into a 48 μm focus at the capillary entrance, which optimises coupling into the fundamental capillary mode.

In this thesis, pulse energy, U, and gas pressure, p, as the most easily-variable system parameters, are left variable to allow investigation of their effect on pump pulse and subsequently HHG behaviour. To this end, they are assigned ranges which straddle the divide between the linear-dominated and nonlinear-dominated behaviour domains. Pulse energy is varied over the range $U \in [0.5, 1.2]$ mJ, while pressure is varied over the range $p \in [50, 140]$ mbar, with $(U, p) = (0.5, 50)$ corresponding to mostly linear pump pulse propagation, and $(U, p) = (1.2, 140)$ corresponding to nonlinearity/plasma driven propagation.

The "average case" propagation is the case where both linear and nonlinear effects are important, resulting in particularly interesting temporal behaviour. The pulse energy and gas pressure used to display this behaviour are taken from previous studies and experimental work, such as [2] and [13]. These energy and pressure values, $U = 0.8$ mJ and $p = 100$ mbar, are hereby referred to as "standard parameters", along with the fixed physical system attributes previously mentioned.

1.6 Thesis summary

As the preceeding chapter explains, there is a great need for a system such a capillary-based HHG for a variety of applications and there is still great scope for optimization of such a system. The following chapter will address the theory of HHG in capillaries and provide physical insight into the difficulties and advantages of HHG while providing a broad and thorough theoretical base for understanding the work of this project. Chapter 3 will address more specific problems with optimization of capillary-based HHG systems and present the primary approach and methods used in this thesis and provide justification for much of the methodology employed. Chapter 4 will present the main results of the thesis and anaylse the effectiveness of the statistical model presented. Conclusions about the efficacy of the project will then be drawn and proposals for future investigation presented.

Chapter 2

Theory of HHG in Capillaries

High harmonic generation in capillaries is difficult to explicitly simulate; since HHG operates on a single atom basis, the HHG spectrum generated from each atom, its effect on the pump pulse, and the effects of the forward and backward propagating XUV on every atom should, in principle, be calculated for each atom of gas in the capillary. Luckily there are a few approximations which can reduce this into a set of discrete steps:

- The pump laser is assumed to be very intense, which means that HHG effects on its propagation are negligible and hence the pump pulse propagation can be considered independently and requires only knowledge of the capillary dispersion and gas nonlinearities.
- The system is assumed to be circularly symmetric. This removes a large proportion of the complexity from the system and allows the propagation and generation to be considered in 1D with simplified waveguide dispersion and severely reduced number of calculations required for a 2D capillary output.

With these approximations in place, the pump pulse propagation and subsequent HHG are modelled in three distinct stages. First is pump pulse propagation which calculates the effect of the capillary waveguide and enclosed gas on the pump pulse as it propagates, taking into account the capillary dispersion and gas nonlinearities. This step produces the electric field of the pulse and associated generated ionisation profile at every spatial point and time along the capillary.

Next the HHG process, based on the already-calculated pump pulse and ions, is simulated and the generated harmonics at each point in the capillary are calculated. Finally, these harmonics are then propagated to the end of the capillary, being shaped by the absorption of the gas and the phase of the generated spectra, predicting the cumulative harmonic output of the capillary.

2.1 Pulse propagation

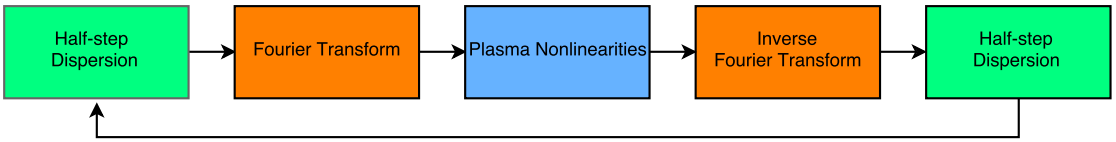

Figure 2.1: Flow chart showing the processes that form the basis of a nonlinear pump pulse propagation through a gas-filled capillary.

As a pulse propagates through a gas-filled capillary, there are several physical effects which shape its evolution. The largest effects come from the capillary dispersion, the gas nonlinearities, and the dispersion and absorption from any generated plasma. These shape the pulse and lead to many interesting features which aid effective HHG. The major steps involved in simulating pump pulse propagation are shown in figure 2.1 and the steps explained in the following sections.

2.1.1 Waveguide modes

Transverse waveguide modes are a linear basis of stable 2D electric field patterns found in waveguides which can propagate in the guiding direction, each with a different propagation velocity.

In capillary waveguides, there are an infinite number of possible modes, of which a limited number (usually the lowest order modes) are excited. The number of possible excited modes can also be narrowed in this case; since the pump beam is assumed to be linearly polarized and coupled into the capillary on-axis, symmetry requires that only the circularly-symmetric linearly polarized modes, $\{LP_{0,m}\}$, can be excited. For simplicity, they are labelled $\{F_m(r)\}$ and their form is given by [37]:

$$F_m(r) = J_0(u_{0m}r/R)/N_m$$

Here $J_0(x)$ is the zeroth-order Bessel function of the first kind and u_{0m} is its mth root. R is the capillary radius and N_m is the normalization for the mth mode.

The modes contain a variable proportion of the pump pulse over the course of the pulse duration, which also varies over the course of the propagation. To describe this variation, functions describing the amount of pump field coupled into each mode, the mode envelope functions, $\{A_m(z,t)\}$ (or in the frequency domain, $\{\tilde{A}_m(z,\omega)\}$) can be constructed. The full pump pulse can then be described by the superposition of modes and their envelope functions, as shown in equation 2.1, taken from [2]:

$$\mathbf{E}(r,z,t) = \frac{1}{2}\sum_m \int d\omega F_m(r) e^{i\beta_m(\omega)z} \tilde{A}_m(z,\omega) e^{-i\omega t} + c.c. \tag{2.1}$$

Here $\beta_m(\omega)$ is the propagation constant for the mth mode and *c.c.* denotes the complex conjugate of the preceding expression. As this equation shows, the only components which are z-dependent are the mode evolution operator $e^{i\beta_m(\omega)z}$, and the mode envelope functions $\{\tilde{A}_m(z,\omega)\}$; although because $e^{i\beta_m(\omega)z}$ has such a trivial dependence on z, the evolution of the coupled pump pulse can be described purely in terms of the evolution of the mode envelope functions, $\{\tilde{A}_m(z,\omega)\}$. At launch, the coupling into each mode is calculated by the mode overlap between the incoming pump and the capillary modes: $\xi_m = \int F_m(r)E_p(r)rdr$, where $E_p(r)$ is the radial profile of the incoming pump beam. Thus,

$$A_m(z=0,t) = \frac{\xi_m}{\Xi}\sqrt{P_0}\exp[-\frac{1}{2}(t/T_0)^2] \tag{2.2}$$

Here $T_0 = 2\sqrt{\log(2)}T_{\mathrm{FWHM}}$ is the pulse width, $P_0 = U_{\mathrm{pulse}}/(T_0\sqrt{\pi})$ is the pulse peak intensity and U_{pulse} is the pulse energy. $\Xi = \sqrt{\sum_m \xi_m^2}$ is a normalization factor for the coupling coefficients.

For simplicity, the field is assumed in the following to couple directly into the lowest order mode, $F_1(r)$, with 100% efficiency, resulting in initial single mode behaviour, although in reality a small proportion of the field couples into higher order modes for all possible Gaussian beam inputs.

2.1.2 Capillary dispersion

Capillary dispersion is a defining feature of this approach to HHG. It not only keeps the beam collimated while propagating through the gas, but also aids in self-compression of the pump pulse, which allows for more intense pulses and hence higher harmonics. The dispersion also allows the capillary to support a very large number of modes at near-infrared (NIR) frequencies. These, combined with the nonlinearities discussed in section 2.1.3 allow mode overlaps and the various mode propagation rates to generate isolated ultrashort pulses within the pump pulse which act as isolated HHG centres, generating large amounts of XUV radiation in short bursts.

The effect of the capillary dispersion on the propagating pulse over a distance δz for each mode, for each frequency, is given by $\tilde{A}_m(z+\delta z,\omega) = \exp[i\hat{\tilde{D}}\delta z]\tilde{A}_m(z,\omega)$, where $\hat{\tilde{D}}$ is the dispersion operator which describes the propagation constants for each mode, as given by [37]:

$$\hat{\tilde{D}} = \frac{\omega}{c}\left\{1 - 0.5\left[\frac{u_{nm}c}{\omega R}\right]^2\left[1 - \frac{2in_g(\omega)c}{\omega R}\right]\right\} \tag{2.3}$$

where R is the capillary radius, u_{nm} is the mth root of $J_{n-1}(u_{nm}) = 0$, and $n_g(\omega)$ is the refractive index profile of the capillary glass.

2.1.3 Gas nonlinearities

Outside of harmonic generation, the gas used in the capillary has a great effect on the propagation of the pump pulse. The effects, along with the capillary dispersion, provide the primary mechanisms for pulse shaping though mode coupling and nonlinear propagation rates. The first gas effect comes in the form of the nonlinear response of the neutral gas, given by [2]:

$$\hat{N}\{A_m(z,t)\} = in_2\frac{\omega_0}{c}\left[1 + \frac{i}{\omega_0}\frac{\partial}{\partial t}\right]\sum_{jkl} S_{mjkl}A_j(z,t)A_k(z,t)A_l^*(z,t) \tag{2.4}$$

where n_2 is the nonlinear refractive index of the gas, ω_0 is the central laser frequency, c is the speed of light, and $S_{mjkl} = \int dxdyF_mF_jF_kF_l$ are the set of mode overlap integrals. With sufficient gas pressure, this response has significant influence on the mode coupling and self-steepening that drives the generation of intense isolated peaks within the pump pulse, although at the pressures and intensities being considered in this thesis, this effect is dwarfed by the other gas effects.

In the high intensity ($\sim$ PW/cm^2), low pressure ($\sim$ 100 mbar) regime being investigated, the significant levels of plasma generated by the pump pulse (see section 2.2.1) result in another major source of mode coupling and self-steepening. This arises from the dispersive effect of the generated free electrons and their collectively highly dispersive and nonlinear electric fields, and is given by [2]:

$$\hat{P}\{A_m(z,t)\} = -\frac{i\omega_0}{2c}\left[1 - \frac{i}{\omega_0}\frac{\partial}{\partial t}\right]\int dxdy\ F_m^*\mathbf{E}(\mathbf{x},t)\frac{\omega_{pl}^2(\mathbf{x},t)}{\omega_0^2} \tag{2.5}$$

where ω_{pl} is the plasma frequency (the mean frequency for oscillations in electron density in a generated plasma), $\{F_m^*\}$ is the set of normalised mode functions for the capillary and $\mathbf{E}(\mathbf{x},t)$ is the spatially, temporally, resolved electric field of the pulse (eq 2.1).

The other nonlinear effect of the generated plasma is absorption arising from the plasma dynamics, which, again, due to its nonuniform strength, provides significant mode coupling and aids in pulse shaping, especially in the high pulse energy/high pressure regime. It is given by [2]:

$$\hat{PL}\{A_m(z,t)\} = -\frac{1}{2}\int dxdy\ F_m^*\mathbf{E}(\mathbf{x},t)\frac{\sum_q \rho_q(\mathbf{x},t)W_q(\mathbf{x},t)U_q}{|\mathbf{E}(\mathbf{x},t)|^2} \tag{2.6}$$

here W_q is the ionization rate for atoms in the qth ionization state ($q \in \mathbb{N}_0$), with ion densities ρ_q, and ionization energies U_q.

Between them, these nonlinearities drive the nontrivial pump pulse propagation which gives the high intensities and particularly high harmonics that are characteristic of the capillary approach to HHG.

2.1.4 Numerical model and simulation details

The pump pulse propagation simulation, based on the work of [41], propagates the mode-decomposed pulse field by evaluating small z-steps of size Δz sequentially along the propagation direction. In each step, a split-step Fourier method is used to evaluate the dispersion in the frequency domain, while the gas nonlinearities are evaluated by a Runge-Kutta-Fehlberg method. The latter method allows for high-order estimation of the nonlinearities' effects, while producing an estimate of the error involved. This error estimate allows for adaptive step size to compensate for $\Delta z \gg 0$, since the split-step method assumes $\Delta z \to 0$; it also allows for consistent error control and allows a minimal number of steps to be used, greatly increasing efficiency.

The algorithm follows the following basic structure for each z step:

- δz, a small portion of Δz, is defined as a first approximation to a "sufficiently small" step size
- the field is operated on by $\exp(0.5i\delta z\hat{\tilde{D}})$ (as in equation 2.3) in Fourier space to make up half a step of dispersion's effect, adding an order of accuracy over a full step of dispersion.
- the field is operated on by $\hat{P} + \hat{PL}$ (equations 2.5 and 2.6), which is evaluated by the Runge-Kutta-Fehlberg (RKF) method.
- If the error estimated by RKF is too high, the z step is repeated using a smaller δz.
- The field is transformed back into Fourier space to apply another $\exp(0.5i\delta z\hat{\tilde{D}})$ as the second half of the dispersion's effect.
- These steps are repeated until $z + \Delta z$ is reached.

δz can be almost equal to Δz for the early propagation because there is little nonlinearity and hence the change in the electric field of the pulse along the propagation, $\frac{\partial E}{\partial z}$, is

small, allowing a whole Δz to be sufficiently small to remain within the $\delta z = \Delta z \to 0$ approximation.

In later propagation, however, there are more isolated intensity spikes and generally more nonlinear behaviour ($\frac{\partial E}{\partial z}$ becomes large). In this case $\delta z = \Delta z$ is far outside the realm of $\delta z \to 0$ which leads to many required steps and hence high computational cost as $\delta z \ll \Delta z$.

2.1.5 Pulse propagation examples

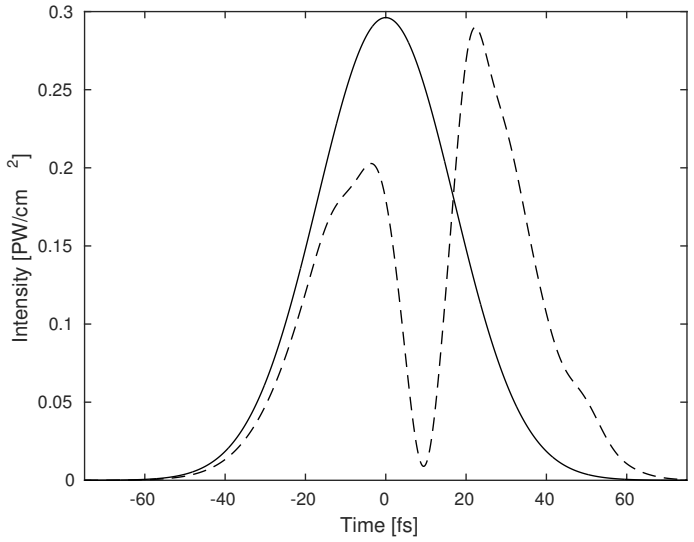

Figure 2.2: Figure showing the initial (–) and final(- -) intensity profiles of a 0.6 mJ pulse propagated through at 7 cm capillary with 100 mbar argon.

Figures 2.2 and 2.3 show initial and propagated pulses for initial pulse energies of 0.6 and 1.2 mJ, respectively, propagating in 100 mbar argon, showing the typical evolution of an intense pulse in the system. These plots also highlight the extent to which higher levels of nonlinearity from the increase in pulse energy lead to extreme changes in the trailing-edge propagation leading to a very non-trivial intensity profile.

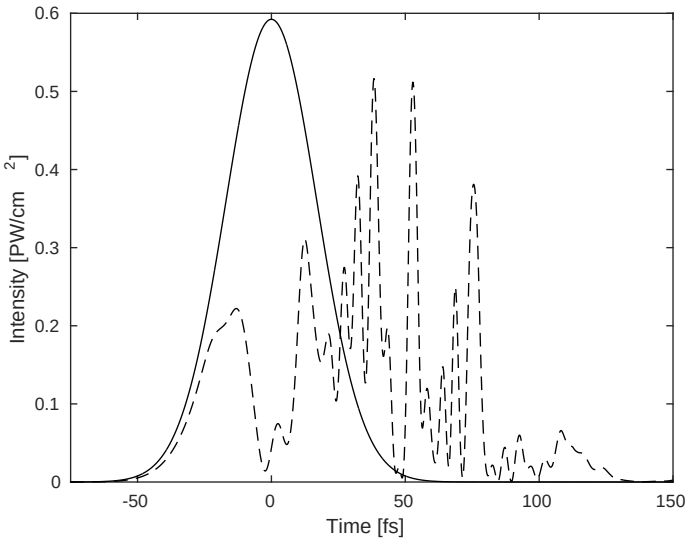

Figure 2.3: Figure showing the initial (–) and final(- -) intensity profiles of a 1.2 mJ pulse propagated through at 7 cm capillary with 100 mbar argon.

2.2 High-Harmonic Generation theory

Calculating the XUV radiation generated from an intense pulse propagation requires the process be split into two main steps: ionization of the gas atoms' outer shell electrons and then their acceleration and recombination. These processes can be considered almost entirely separate and in fact the level of ionization is calculated in the pulse propagation stage of simulation and is used to calculate the plasma nonlinearities in equations 2.5 and 2.6; because the ionization processes occurring are quite different from the standard single-photon ionization processes, they are detailed in the following section 2.2.1.

The post-ionization acceleration and recombination portions of the HHG process are detailed in section 2.2.2, providing insight into the actual mechanics of the process. This process, as described later, is computationally inefficient to simulate and so a semi-classical model which approximates the underlying physics is used and descibed in section 2.2.3.

2.2.1 Tunnel/multiphoton ionization

Ionization usually occurs when an electron bound at energy E_I in an atom is excited by a photon with energy $E > E_I$, ejecting the electron. For a gas such as Argon, this would require a photon of wavelength < 78 nm, which are difficult to consistently generate.

In cases where such high energy photons are not present, ionization can still occur through absorption of multiple photons of $E < E_I$, which can be done in two ways:

Multiple photons can be absorbed simultaneously, as long as their combined energy is greater than E_I, as in figure 2.4. This is common in high-intensity pulses where there are a lot of photons colliding with an atom at any give time. Multiphoton ionization can also happen incrementally, with subsequent excitations putting the electron in stable higher energy states, until eventually its energy exceeds E_I. This does require a wide spectrum containing photon energies corresponding to the particular transition energies of an atom, and a large flux to ensure that the probabilities of mass excitation are non-negligible.

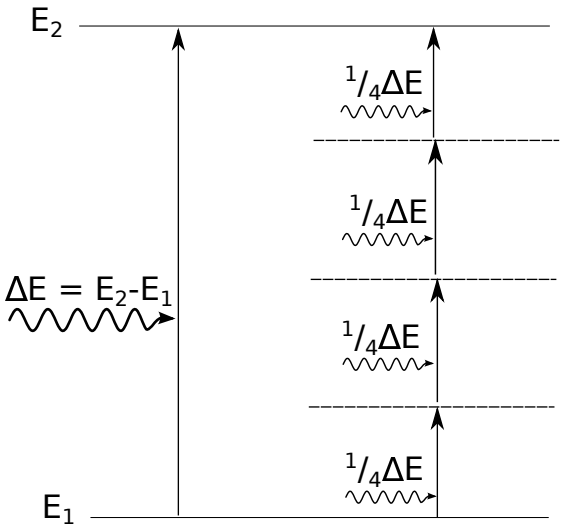

Figure 2.4: Energy level diagram showing the transition between bound state E_1 and continuum state E_2 by absorption of a photon of energy $\Delta E{=}E_2{-}E_1$, and the same transition achieved by the absorption of four photons of energy $\frac{1}{4}\Delta E$, with dashed lines denoting virtual states with energies $E_1 + \{\frac{1}{4}, \frac{1}{2}, \frac{3}{4}\}\Delta E$. These virtual states are simply an example and typically multiphoton ionization occurs through absorption of photons of differing energies and total energy $> \Delta E$

The other method of ionizing electrons with photons of energy $E < E_I$ is through tunnel ionization, as seen in figure 2.5. In this case, an intense, fast-varying field can distort the atomic potential. With sufficient intensity, the potential on one side of the atom becomes sufficiently low that an electron, or at least part of its wavefunction, can tunnel from its ground state through this potential barrier, resulting in ionization. In this case, the electron's wavefunction does not completely tunnel though the barrier, and hence the electron has a finite chance of existing either in the ground or ionized state, a chance which depends on the level of potential deformation. Because of this deformation dependence, very intense fields are required to ensure a significant ionization rate.

Although the two ionization methods described above are somewhat different, they are not mutually exclusive and are both part of what is fundamentally a single quantum process, as described by Keldysh theory [43], with their relative rates given by the Keldysh parameter $\gamma = \omega/\omega_t = I_p/(2U_p) = |E|^{-1}\omega\sqrt{2m_e I_p}/e$, where $|E|$ is the magnitude of the exciting field, ω is the frequency of the pump laser, ω_t is the electron tunneling frequency

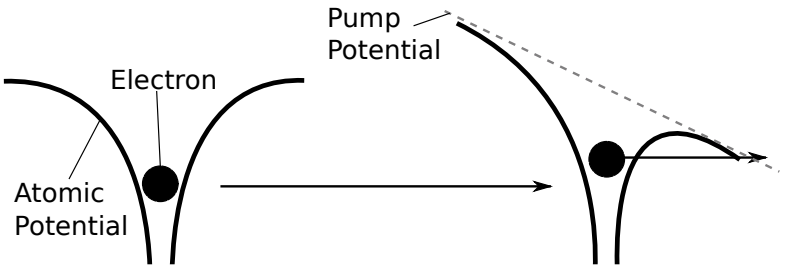

Figure 2.5: Schematic of tunnel ionization showing how deformation of the atomic potential by the pump field allows an outer shell electron to tunnel from its parent atom.

given by the effective potential barrier, and m_e, I_p, U_p, and e are the electron mass, the ionization potential, the ponderomotive energy of the pump field, and the electronic charge, respectively. The two limiting cases of the Keldysh parameter are when one of the two above ionization processes dominates.

When $\gamma \gg 1$, multiphoton absorption dominates because the potential is insufficiently deformed to allow much of the electron wavefunction to exist outside the atom. This is because the tunnelling time is very small compared to the photon frequency, and so tunnel ionization must occur in a very small proportion of the optical cycle, resulting in a low probability of tunnel ionization. Conversely, the high optical frequencies allow many photons to be absorbed in the time taken for a single tunnel ionization.

In the other extreme, $\gamma \ll 1$ and so the tunnelling frequency exceeds the optical frequency, allowing many tunnel ionizations in the time of a single optical cycle. This leaves a large proportion of the electron wavefunction outside the atom in the time a single photon, of the many required for multiphoton ionization, is absorbed.

In the intermediate case ($\gamma \sim 1$), both multiphoton and tunnel ionization occur with similar probabilities, although most systems tend to work at either extreme.

In the system under examination, the pump pulses used typically fulfil the $\gamma \ll 1$ condition and so the ionization rate for transitions from unionised to the 1+ ionization state is given by [43]:

$$W(t) = \kappa^2 \sqrt{\frac{3}{\pi}}\, C_{kl}^2\, 2^{2n^*}\, F(t)^{1.5-2n^*}\, \exp\left[-\frac{2}{3F(t)}\right] \tag{2.7}$$

$$C_{kl}^2 = \frac{2^{2n^*-2}}{n^*\, n^*!(n^*-1)!} \tag{2.8}$$

Here $F(t) = |E(t)|/\kappa^3 E_a$ is the reduced field, where E is the electric field of the pump pulse, $\kappa^2 = I/I_H$ is the ratio of the ionization energy, I, to the ionization energy of

hydrogen, $I_H = 13.6$ eV. $E_a = 5.14 \times 10^9$ V cm^{-1} is the atomic unit of electric field intensity. $n^* = Z/\kappa$ is the effective quantum number, with Z being the atomic number. Figure 2.6 shows the fraction of 1+ and 2+ ions generated from a single pass of a 0.395 PW/cm^2 40 fs pump pulse, illustrating how abruptly a large proportion of ions can be generated and the typical shape of $W(t)$ for short times. The fraction is assumed to return to zero between pulses. As the figure shows, the level of 2+ ionization is very low even in the most nonlinear cases and so it is ignored for the simulations performed in this thesis. Also it must be noted that equations 2.7 and 2.8 are written with the assumption that only the lowest energy bound electrons are ionized, which is a reasonable assumption given that the lowest energy electron is by far the most likely to be ionized first and, as figure 2.6 shows, the proportion of 2+ ions generated is extremely small.

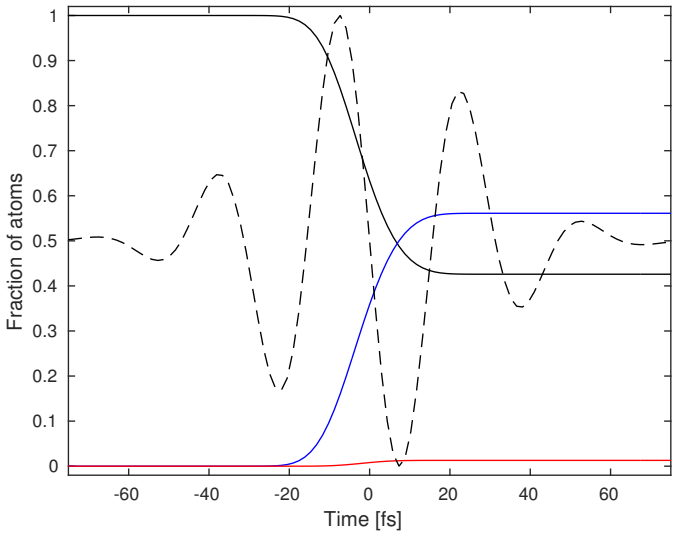

Figure 2.6: Figure showing the imaginary component of a typical pump pulse (- -) of 0.395 PW/cm^2 intensity and 40 fs length; the fraction of 1+ and 2+ ions it generates, (–) and (–), respectively; also the fraction of neutral atoms (–) illustrating how abruptly and efficiently such a pulse can generate a large proportion of ions.

2.2.2 HHG Theory - Quantum model

After ionization by either of the above processes occurs a portion of the electron wavefunction exists, disconnected from a parent atom, in the intense driving field. The part of the electron wavefunction which left the atomic potential experiences nonlinear acceleration from the intense, rapidly varying driving field, known as the ponderomotive force. This force arises from the high intensity oscillations of the driving field, and when averaged over an optical cycle is proportional to $^I/_{\omega^2}$, where I is the field intensity, and ω is the frequency of the field. Because of its nonlinear nature, this acceleration can provide a lot of energy to the ionized electron. For example a PW/cm^2 intensity field

at 800 nm can provide up to $\sim$ 60 eV to the electron, or the equivalent of absorbing 39 photons, making the process extremely efficient compared to acceleration by absorption.

After acceleration, the ionized portion of the wavefunction's energy increases significantly. Assuming that the driving field is linearly polarized to a good approximation, the ionized portion of the wavefunction recombines with its parent atom, and with the remaining unionized, still-bound, potion of the electron's wavefunction. The recombination of these two components of the electron wavefunction, one bound and one intense and planar, cause fluctuations in the charge density of the wavefunction. Such charge density fluctuations radiate as a dipole, causing photons with energy much greater than those in the driving field, to be released. This is the basic single-atom harmonic spectrum.

The time-dependent Schrödinger equation (TDSE) describing the system is as follows:

$$i\hbar\frac{\partial}{\partial t}|\Phi(\mathbf{x},t)\rangle = \left[-\frac{\hbar^2}{2m_e}\nabla^2 + \mathbf{V}_{atom}(\mathbf{x}) + \mathbf{V}_{field}(\mathbf{x},t)\right]|\Phi(\mathbf{x},t)\rangle \tag{2.9}$$

Here $|\Phi(\mathbf{x},t)\rangle$ is the electron wavefunction, m_e is the electronic mass, $\mathbf{V}_{field}(\mathbf{x},t)$ is the potential of the driving field, and $\mathbf{V}_{atom}(\mathbf{x})$ is the atomic potential.

The atomic potential is usually taken to be of the soft coulomb form $\mathbf{V}_{atom}(\mathbf{x}) = -V_0[\alpha + \mathbf{x}]^{-1}$, where V_0 is the first ionization energy of the atom while α is a regularization parameter which should be small, with value usually equal to the Bohr radius.

Such a process can only generate odd-numbered harmonics from centrosymmetric particles, such as atomic Argon, because the time averaged response from a symmetric atomic potential due to a single optical cycle is zero due to symmetry considerations, whereas in a non-centrosymmetric potential would result in a non-zero time averaged force over an optical cycle. Over a half-cycle of excitation, however, the time-averaged force is necessarily positive, resulting in generation of odd harmonics, since even harmonics require the interaction of the centrosymmetric potential and $\mathbb{N}$ full optical cycles and hence no net force.

The field is then subject to phase matching between the frequency components generated, in which only the frequency components near each harmonic are efficiently propagated, due to the phase difference Δk, between the wavevectors of the harmonic and the fundamental frequency being near zero. The phase difference in vacuum, is given by:

$$\Delta\mathbf{k} = \mathbf{k}_h - q\mathbf{k}_1$$

here $\mathbf{k}_h$ is the wavevector of the q^{th} harmonic, and $\mathbf{k}_1$ is the wavevector of the pump laser. Given this, the HHG spectrum generated from a monochromatic pump laser will

resemble the spectrum shown in figure 2.7 [32]; although for any pulsed pump laser, like the one used, there will be a wide spectrum in the pump laser and hence the discreteness of the spectrum will become less pronounced as the pump pulse spectrum widens, as seen in the spectrum calculated from theory in figure 2.8, and its wide and noisy harmonics.

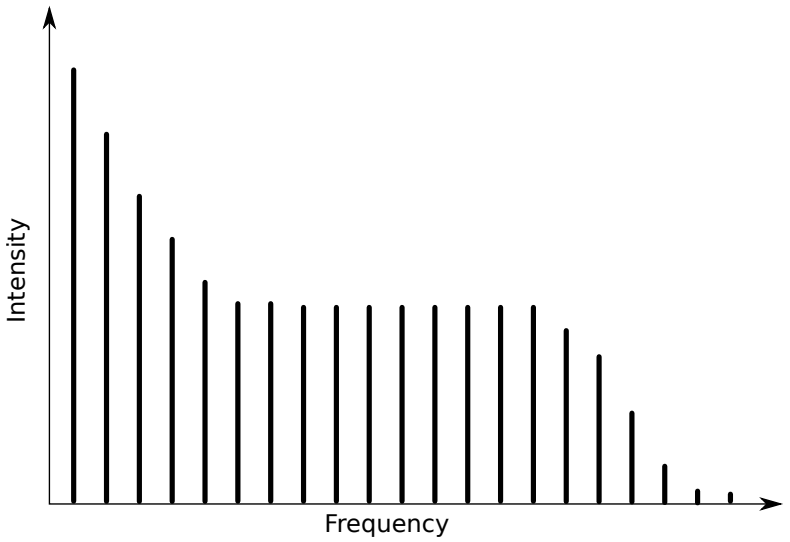

Figure 2.7: Schematic plot showing the typical features of a HHG spectrum from a monochromatic source, with characteristic discrete intensity spikes at each odd harmonic of the source wavelength, the intensity plateau region, and the subsequent harmonic cutoff and falloff, whose position is given by equation 2.11.

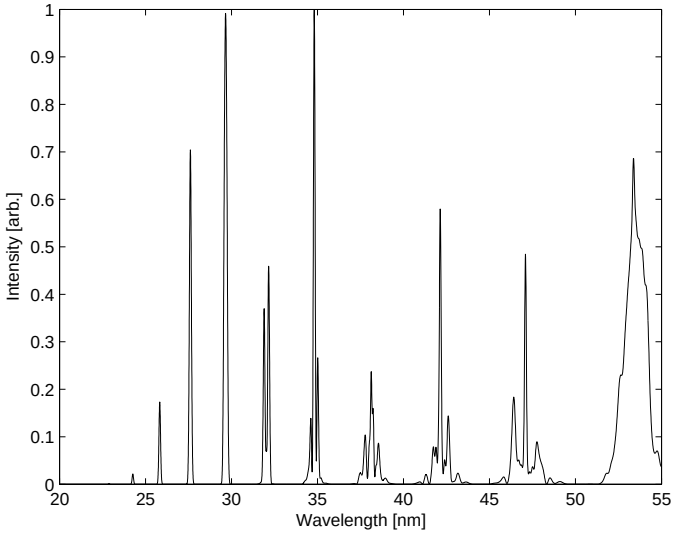

Figure 2.8: Plot of the 20-55 nm wavelength section of the HHG spectrum generated by the interaction of a 0.1 PW/cm^2, 40 fs 800 nm pulse with a single argon atom. It shows the effect of generation from a wide pump bandwidth in the nontrivial harmonics shapes and associated wings which come from the large variety of pump frequencies.

2.2.3 HHG Theory - Semi-classical model

For simulation efficiency, explicit HHG simulations over the course of this work were done using a semi-classical approximation to the quantum model seen in the previous section. This model, based on the work of [35], including generalizations of [44] and [17], takes a three-step model approach to HHG where the process is broken down into ionization, acceleration, and recombination; as seen in figure 2.9. The latter two steps are calculated together on a single-atom basis and fully determine the generated HHG spectrum, whereas the ionization merely provides total numbers of generating atoms, since a strong-field approximation (SFA) ensures that ionization removes a negligible amount of energy from the pump field, allowing pulse propagation to be considered separately.

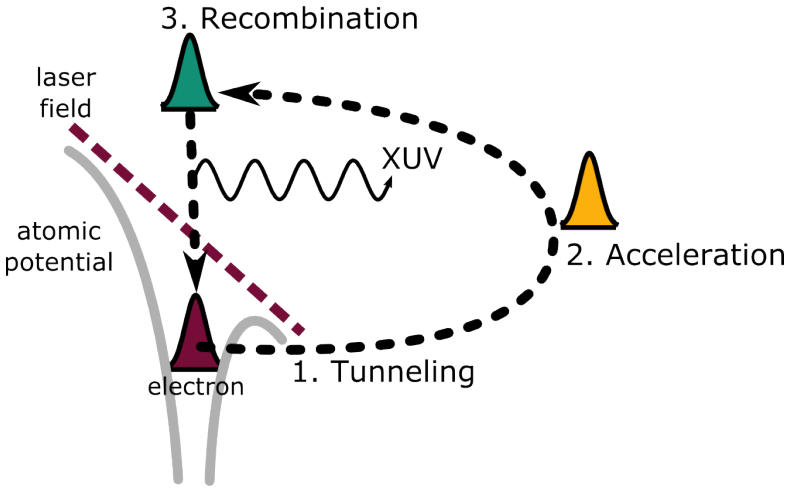

Figure 2.9: Figure showing the three-step model of HHG. It describes the tunnel ionization of the electron, subsequent acceleration in the pump field and finally recombination with its parent atom and emission of XUV. [att: MDSwo / CC BY-SA 3.0]

This model takes the electron as a nonlinear oscillator, which allows for easy calculation of momentum and action across the bound state to continuum transition for calculating recombination energies. The atom itself is modelled as hydrogenlike which is usual in the semiclassical approximation [35], with bound state to continuum state transition dipole matrix element given by [45]:

$$d(p) = i\frac{2^{7/2}(2I_p)^{5/4}(\hbar\omega_0)^{7/8}e}{\pi m_e \omega_0}\frac{p}{(p^2/(2m_e)+2I_p)^3}$$

Here $p_{st} = \frac{e}{t'-t}\int_{t'}^{t} A(t'')dt''$ is the electron's momentum, e it's charge, and m_e it's mass, $A(t)$ is the vector potential of the pump field, and I_p is the atom's first ionization energy. The generated dipole strength, $x_{nl}(t) = \langle\Phi(x,t)|x|\Phi(x,t)\rangle$, for a single atom is then given by [44]:

$$x_{nl}(t) = \mathrm{Re}\Big[\frac{i}{\hbar}\int_{-\infty}^{t} dt' \left(\frac{\pi}{\epsilon + i\omega_0(t-t')/2}\right)^{3/2} d^*[p_{st}(t',t) + eA(t)]d[p_{st}(t',t) + eA(t')]\mathrm{e}^{-iS_{st}(t',t)}E_p(t')\Big] \quad (2.10)$$

Here $E_p(t)$ is the electric field of the pump pulse, ϵ is a small regularization constant, introduced to avoid poles, and $S_{st}(t',t) = [(t-t')(I_p - p_{st}^2/(2m_e)) + \frac{e^2}{2m_e}\int_{t'}^{t} A^2(t'')dt'']/\hbar$ is the stationary action integral. The source term for the radiation at a given point in the propagation is then given by $\tilde{P}_{dip}(\omega) = \widetilde{FT}[N_{atom}(t)x_{nl}(t)]$, where $\widetilde{FT}$ denotes a Fourier transform, and $N_{atom}(t)$ is the neutral atom density across the time window.

Calculating the dipole source terms in equation 2.10 requires integration of the electric field and its potential over all history. In reality this can be reduced by examining the kinetic energy gain of the electron by ponderomotive acceleration from the pump pulse. This is given by considering the electron as a particle in a linearly polarized oscillating field:

$$m_e\ddot{x} = eE\cos(\omega_0 t)$$

Here m_e is the electron mass again, $\ddot{x}$ is the acceleration of the particle, e is the electronic charge, E is the amplitude of the pulse electric field, and ω_0 is the pump field frequency. After ionization, $\dot{x}(t_0) = x(t_0) = 0 \implies \dot{x}(t) = \frac{eE}{m_e\omega}(\sin(\omega_0 t) - \sin(\omega_0 t_0)) \implies$

$$x(t) = \frac{eE}{m_e\omega^2}[-\cos(\omega_0 t) - \omega_0 t\sin(\omega_0 t_0) + \cos(\omega_0 t_0) + \omega_0 t_0\sin(\omega_0 t_0)]$$

From this, and considering that only paths which return to $x = 0$ generate harmonics, the kinetic energy of any returned electron is given by:

$$E_{kin} = 2\frac{e^2E^2}{4m_e\omega^2}\left[\sin(\omega_0 t) + \frac{\cos(y) - \cos(\omega_0 t_0)}{\omega_0 t - \omega_0 t_0}\right]^2$$

$U_p = \frac{e^2E^2}{4m_e\omega^2}$ is the aforementioned ponderomotive energy imparted by the pump field, and so the kinetic energy gain per unit ponderomotive energy,

$$E_{kin}/U_p = 2\left[\sin(\omega_0 t) + \frac{\cos(y) - \cos(\omega_0 t_0)}{\omega_0 t - \omega_0 t_0}\right]^2$$

This can be optimized to find the maximum possible energy gained this way. The optimal t_0 and subsequently the optimal path for kinetic energy gain is given by the solution to the following:

$$0 = \frac{\sin(\omega_0 t_0)}{\omega_0 t - \omega_0 t_0} - \frac{\cos(\omega_0 t_0)}{(\omega_0 t - \omega_0 t_0)^2} + [\cos(\omega_0 t) - \frac{\sin(\omega_0 t)}{\omega_0 t - \omega_0 t_0} + \frac{\cos(\omega_0 t_0)}{(\omega_0 t - \omega_0 t_0)^2}] \frac{(\omega_0 t - \omega_0 t_0)\cos(\omega_0 t_0)}{\sin(\omega_0 t) - \sin(\omega_0 t_0)}$$

This equation is solved for $\omega t_0 = 17.956°$, resulting in a kinetic energy gain per unit ponderomotive energy of 3.17, as shown by figure 2.10.

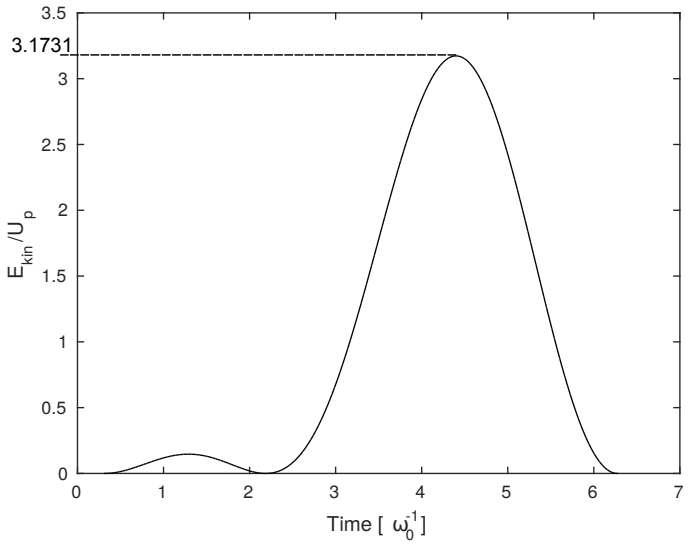

Figure 2.10: Plot of the kinetic energy gain of a free electron as a function of time of flight in the semi classical model of electron acceleration by the pulse field for the optimal ejection phase angle $\omega t_0 = 17.956°$. Note that the peak kinetic energy gain is $3.1731U_p$, indicating the maximum kinetic energy that an electron can gain from ponderomotive acceleration before recombination.

As seen in figure 2.10, by 2 optical cycles, the maximum kinetic energy has long been gained by the electron. To this end, only the first 3 optical cycles will be considered when calculating $x_n(t)$, since dipole strengths calculated over four or five cycles contribute negligible extra energy. The maximum kinetic energy gain of the electron of $3.17U_p$ allows for calculation of the highest energy harmonic photons that could be produced:

$$N_h \lesssim \left[I_P + 3.17 \frac{e^2 I}{2c\epsilon_0 m_e \omega_0^2} \right] / \hbar\omega_0 \tag{2.11}$$

Here N_h is the maximum possible harmonic, I_P is the first ionization energy of the gas being used, It should be noted that the derivation for this expression assumes $U_p \gg I_p$, and so this expression is a bad approximation for $U_p \approx I_p$ or pump intensity $I_{max} <$ 83.2 TW/cm^2 for 800nm pump, and so this approximation should only be used when expecting harmonics of >20.

2.2.4 XUV propagation

Despite propagating through the same system, the pump pulse and generated XUV have very different propagation properties. For example, because the XUV has frequencies far greater than the plasma frequency, the plasma-induced effects are very minimal on the XUV and can be ignored. Similarly with the neutral gas nonlinearity and dispersion; since the wavelengths of the XUV are many orders smaller than the capillary radius, the effects of the capillary and the mode structure become negligible. The one thing that does have a significant effect on the XUV propagation is the absorption of the neutral gas. Since the pump wavelengths are well above the K-absorption edge of argon ($\sim$ 78 nm), the linear absorption from the neutral argon is negligible; but in the XUV region there are very severe regions of absorption, as seen in figure 2.11, which have a very large effect on the cumulative XUV pulse. As the XUV from each single-atom propagate, they combine to form a full HHG spectrum.

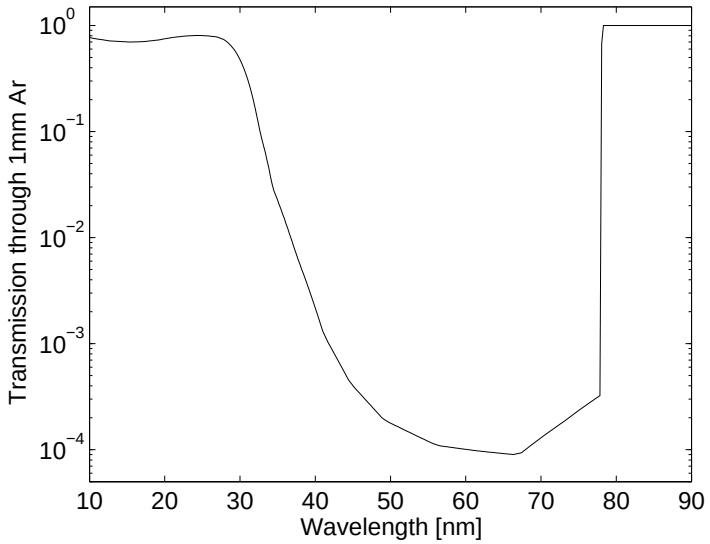

Figure 2.11: Plot of the transmission spectrum of 1mm of Ar at 100mbar. Note the high transmission around 30nm, which is key in harmonic spectrum shaping. This spectrum is generated by various atomic models by CXRO [http://henke.lbl.gov/optical_constants/]

Combining the effects of phase matching and the gas absorption, as well as radial movement, the harmonics' cumulative field behaves according to the following differential equation[17]:

$$\nabla_{\perp}^{2}\tilde{E}_h(\omega)+\frac{2i\omega}{c}\frac{\partial\tilde{E}_h(\omega)}{\partial z}+\frac{i\omega}{c}\tilde{\alpha}(\omega)\tilde{E}_h(\omega)=-\frac{\omega^2}{\epsilon_0 c^2}\widetilde{FT}[N_{atom}(t,z)x_{nl}(t,z)] \qquad (2.12)$$

here $\tilde{E}_h(\omega)$ is the harmonic spectrum, $\tilde{\alpha}(\omega)$ is the argon absorption spectrum as seen in figure 2.11, $N_{atom}(t,z)$ is the density of neutral atoms across the temporal window, $x_{nl}(t,z)$ is the set of dipole strengths generated across the pulse, as calculated in section 2.2.3, and $\widetilde{FT}[N_{atom}x_{nl}]$ denotes a Fourier transform of $N_{atom}x_{nl}$ from t to ω space.

Since every atom at a given time can be thought of as a point source emitting in the $+z$ direction and the Rayleigh length of the XUV is much longer than the capillary length, $\nabla_\perp^2 \tilde{E}_h(\omega)$ can be considered zero, which leaves the harmonic propagation as an integration over z:

$$\tilde{E}_h(\omega,z) \approx e^{-\frac{\tilde{\alpha}(\omega)z}{2}} \int_0^z e^{\frac{\tilde{\alpha}(\omega)z'}{2}} \widetilde{FT}[N_{atom}(t,z')x_{nl}(t,z')]dz' \tag{2.13}$$

The XUV propagation is hence reduced to a series of planes, perpendicular to the propagation direction, which accumulate linearly along the propagation.

2.3 Theory Summary

In the preceeding pages we have introduced a theoretical basis for the system decribed in section 1.5, covering everything from capillary waveguides and XUV propagation to the physics of HHG and the numerical details of simulations. This theory will be key in understanding the methods employed in future chapters and will provide comparison and physical insight into the results of the novel simulation method detailed in chapter 3, as well as providing the theoretical tools for one to recreate the work found herin.

Chapter 3

Statistical analysis of nonlinear infrared pulse propagation

In this chapter we justify and introduce the novel methods used in the titular statistical description of HHG. These include the algorithms used to subdivide propagating pulses and the methods used to collect and characterise information taken from subdivided pulses. It also introduces many key concepts such as fast and slow fluctuations and their models and statistics, and paves the way for a statistically derived approximation to HHG spectra in chapter 4.

3.1 Features of pump pulse propagation and the need for statistics

As seen in section 2.1.5 and illustrated in figure 3.1, pump pulse propagation is very nontrivial; effects such as the capillary dispersion and nonlinear response of the generated plasma lead to very spiky, complicated behaviour in the pulse's trailing edge. This nontrivial behaviour is dealt with in the simulation by the use of a high resolution temporal grid and very frequent evaluation along the z axis. Although this does allow for high precision evaluation of the pump pulse propagation, it results in extremely long simulation times when calculating the XUV generated from the pulse, which limits the pace of theoretical research.

The nontrivial pulse shape and the fast-varying nature of the pump pulse structure mean that a low-order approximation to the behaviour is insufficient, and sufficiently high-order approximations become inefficient. It must be noted, however, that in a nonlinear optical process such as HHG, pulse peaks have a significantly greater effect than any low intensity regions, and so the behaviour of the pulse, for the purpose of predicting generated XUV through HHG, can be considered as the behaviour of the peaks of that

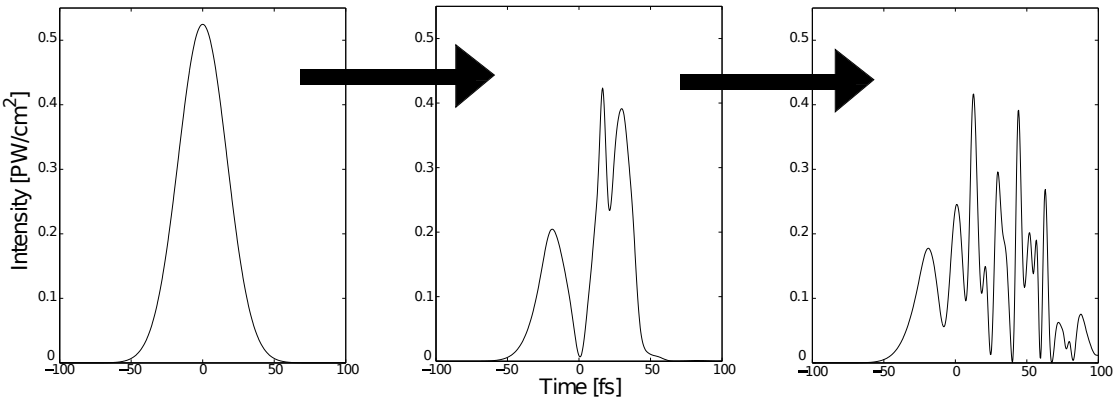

Figure 3.1: Plot showing the intensity profile of a 0.8mJ, 100mbar propagating pulse at launch, 25mm propagation and 50mm propagation. This highlights the pulse breakup and its heavy effect in the pulse's trailing edge.

pulse, since they generate the vast majority of the XUV. It must also be noted that, although important for a single-atom, instantaneously generated spectrum, each of the many peaks in the pulse's trailing edge contains little individual energy, and hence the contribution from each individual peak should be small. There are also enough of these small peaks over the course of a propagation to start considering them as a statistically significant number and distribution of peaks, under the law of large numbers. In this way, the peaks of the propagating pulse can be considered a statistical ensemble, and in accordance with the law of large numbers, the mean HHG spectrum generated from this ensemble should approximate the cumulative HHG spectrum generated by the actual propagating pulse.

This approach should allow calculation of the HHG spectrum generated from a propagating pulse without having to calculate the spectrum generated from each part of the propagating pump pulse at each instant by calculating the average HHG spectrum generated by the ensemble of peaks in the propagating pulse. This should provide an enormous speed advantage over explicit simulation of the HHG process, given that the statistical ensemble of pump pulse peaks is easily calculable and precalculated HHG spectra can be used to describe the spectrum generated from each peak since they have limited intensity and width ranges. The spectrum generated from such statistical analysis should be accurate provided that the system is sufficiently nonlinear and hence there are significantly enough fast-varying peaks with enough width and intensity variance within the pump pulse to fulfil the statistical significance condition of the law of large numbers.

This idea of using statistics to analyse highly nonlinear behaviour is both novel and potentially extremely useful in the active field of highly nonlinear systems. The specific methods employed in this analysis should be widely applicable to other highly nonlinear systems and even if not directly applicable, the ideas from this approach provide a framework for applying such an approach to other systems. The methods used are

documented over the remainder of this chapter and the results from these methods are analysed and compared to explicitly simulated data in the following chapter.

3.2 Pulse deconstruction and subpulse identification

Given that a propagated pulse usually contains multiple sharp intensity peaks separated by very low intensity troughs, and that intensity has a nonlinear effect on generated harmonics, these low intensity troughs should produce negligible XUV, and so they can be effectively ignored.

With the troughs in between intensity peaks ignored, the peaks resemble a discrete train of pseudo-Gaussian pulses which generate XUV independently, known as subpulses. Figure 3.2 shows a typical propagated pulse which has been subdivided into a number of subpulses, which are ordered by their peak intensity.

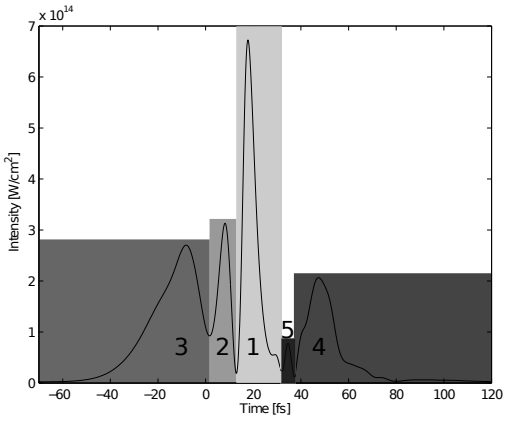

Figure 3.2: Plot of a cropped pulse intensity profile, with the subpulse assignments shown by the shaded areas of decreasing brightness and assignment numbers. The profile is taken from partway along a propagation at "standard parameters", including some coupling into the $LP_{0,2}$ and subsequent modes at launch; and chosen for illustrative purposes.

The pulse deconstruction algorithm for each z position is as follows:

- First the highest peak in the intensity-time profile, is selected and denoted as $I_1(z)$, and the nearest half-intensity points either side are found. The temporal distance between these two points is designated as the full width half maximum (FWHM), $T_1(z)$ of the subpulse.
- The nearest intensity minima outside the FWHM range are then found and designated the edges of the subpulse. The temporal space between these edges is then designated as the subpulse, as shown by the shaded areas in figure 3.2.

- This is then repeated for every intensity peak over 10 TW/cm^2 to give a set of peak intensities, $\{I_n(z)\}$, and FWHMs, $\{T_n(z)\}$, describing the intensities and widths of all n subpulses at a given z.

This algorithm is then repeated for every propagation step, producing $2m$ functions of $I_n(z)$ and $T_n(z)$, where m is the maximum number of subpulses found in a pulse at any point along the propagation. These functions describe the intensity and width evolution of the nth most intense subpulse over the pulse's propagation, which produces behaviour similar to that seen in figure 3.3.

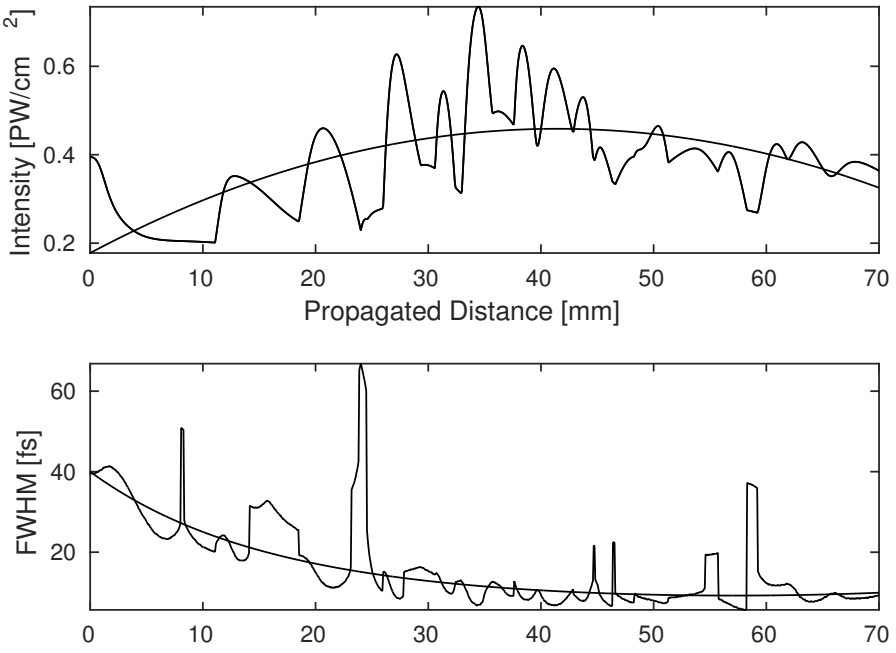

Figure 3.3: Plot of the intensity and width of the primary subpulse at "standard parameters" (see section 1.5), with low-order fits denoting the "average" behaviour over the propagation.

As figure 3.3 shows, the intensity and width of the most intense subpulse vary quite sporadically and quickly, although there are definite long-distance trends. These long distance trends or "slow fluctuations" can be extracted from the propagation to provide a map of the purely short distance, or "fast fluctuations" . The low-order black curves describe these slow fluctuations; they are calculated using a general least-squares fitting algorithm. The functions describing the curves were chosen carefully to provide agreement with the expected long distance behaviour while being of as low order as possible. To this end, the slow fluctuations for a given subpulse are approximated by:

$$\hat{I_n}(z) = a_n z^2 + b_n z + c_n \tag{3.1}$$

$$\hat{T_n}(z) = \exp\left(f_n z^2 + g_n z + h_n\right) \tag{3.2}$$

here a_n, b_n, c_n, f_n, g_n, and h_n are fitting constants for the nth subpulse.

3.3 Fast fluctuations

With the slow fluctuations, $\hat{I}_n(z)$ and $\hat{T}_n(z)$, calculated for each subpulse, the rest of the subpulse dynamics, the fast fluctuations can be exposed and analysed. The slow fluctuations are removed by taking $I_n(z)/\hat{I}_n(z)$ and $T_n(z)/\hat{T}_n(z)$, which should normalise the behaviour of I_n and T_n over the propagation, allowing intensities and widths from different parts of the propagation to be compared on an equal footing. For reasons that are made clear in section 3.7, the fast fluctuations are taken as the cubic root of the previously mentioned ratios:

$$\tilde{I}_n(z) = \sqrt[3]{I_n(z)/\hat{I}_n(z)} \tag{3.3}$$

$$\tilde{T}_n(z) = \sqrt[3]{T_n(z)/\hat{T}_n(z)} \tag{3.4}$$

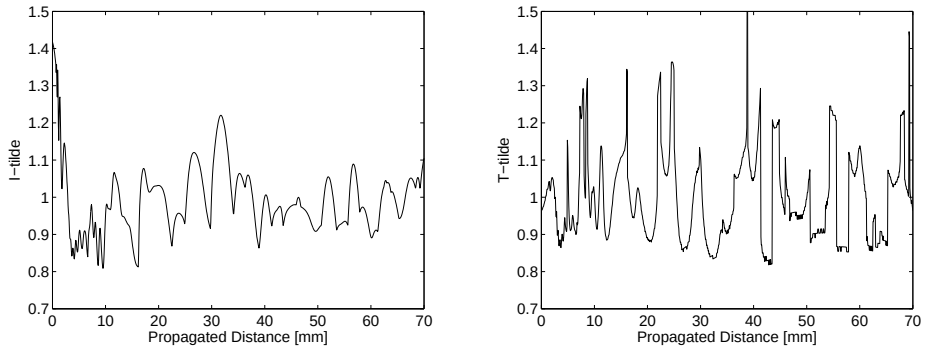

Figure 3.4: Plots of the rescaled intensity and width for the primary subpulse as it propagates at "standard parameters" (0.8 mJ, 100 mbar). Note that the fluctuations are now centred round unity and appear consistent over the propagation.

As figure 3.4 shows, the fast fluctuations are well normalised to an average of unity by the removal of the slow fluctuations, which illustrates these values as fluctuations about another behaviour, similarly to other systems which have behaviours on very different time and distance scales.

3.4 Subpulse counting and intensity/width counting algorithms and evolution

As previously mentioned, as the pump pulse propagates, it breaks up, forming a number of subpulses out of the original Gaussian intensity profile. With a variable number of subpulses, there are potential issues with using a ubiquitous pair of functional forms to describe the intensity and width evolution of every subpulse. To this end, the number of subpulses at each propagation step are counted to form a function $n_{sub}(z)$. This function varies heavily with system parameters such as pulse energy and gas pressure, and so, again, a fit is taken to average out such variance.

Since the number of subpulses is always one at $z = 0$, and appears to grow quadratically for short propagations, a quadratic fit was used, but since the number in the late propagation seems to grow linearly and/or saturate, a cubic term was added to allow for maximum flexibility while keeping the fit order low. The linear term was also found to be very small for most parameter regions, and so was ignored. The chosen fit function is then given by:

$$n_{sub}(z) = \nu z^3 + \tau z^2 + 1$$

here τ describes the rate of growth in the early-mid propagation, while ν describes the late-propagation growth, and indirectly indicates the level of saturation of subpulses within the pulse in the late propagation.

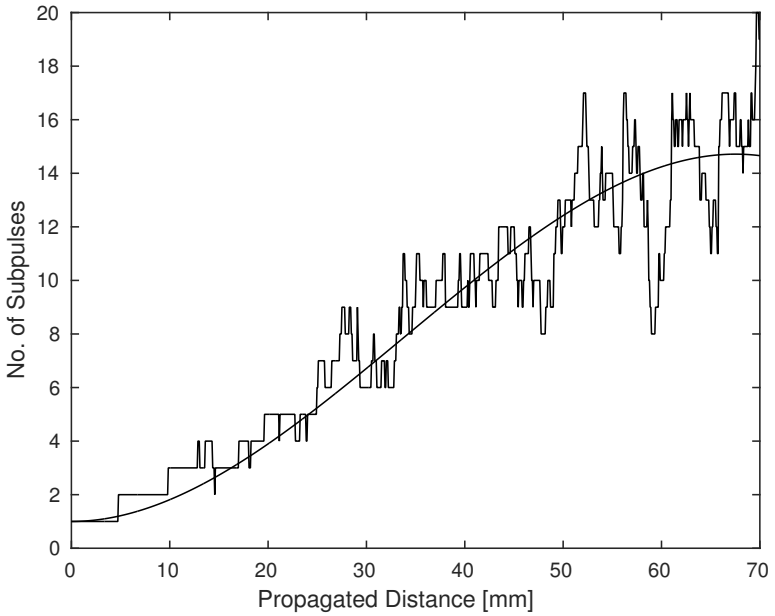

Figure 3.5: Plot of the number of subpulses in the pump pulse as it propagates, showing how the number and variance grow over the course of the propagation, with cubic fit to show its averaging effect.

Naturally the number of subpulses is integer and so the number over the propagation is heavily stepped; this makes a smooth fit even more useful because it averages out the rapid and nonlinear changes in the position at which a given subpulse appears, allowing for smooth "averages" as seen in figures 3.6 and 3.7. These plots also show the stark difference that the pump pulse energy, and hence level of nonlinearity, makes to the pulse breakup, with more than four times the number of subpulses found in the propagated pulse at 1.2 mJ compared to 0.6 mJ and significantly faster growth in the early propagation which is unsurprising given that all nonlinear effects are expected to be significantly stronger in the 1.2 mJ case than at 0.6 mJ and hence the severely increased mode coupling and ionization leads to the increased pulse breakup. Another interesting feature of figure 3.7 is the plateau at ∼60 mm propagation; although the actual number of subpulses does not saturate to this degree, it is symptomatic of a small amount of subpulse saturation within the pulse slowing the growth in subpulse number.

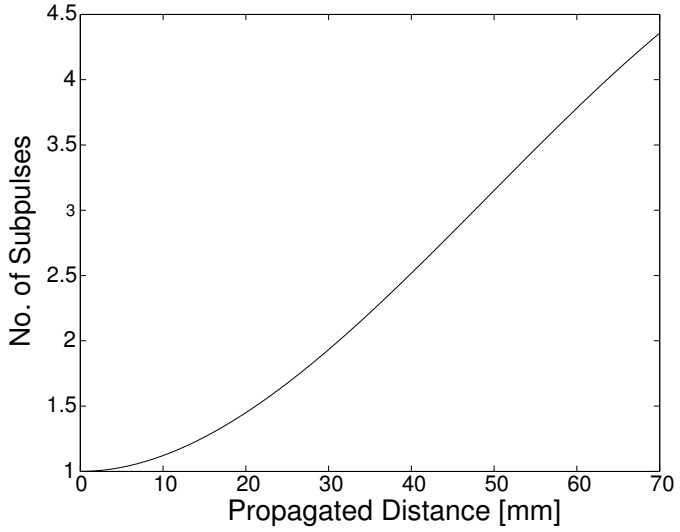

Figure 3.6: Plot showing the expected subpulse number evolution at low energy and low pressure (0.6 mJ, 70 mbar). Note the slow and eventually linear growth in subpulse number.

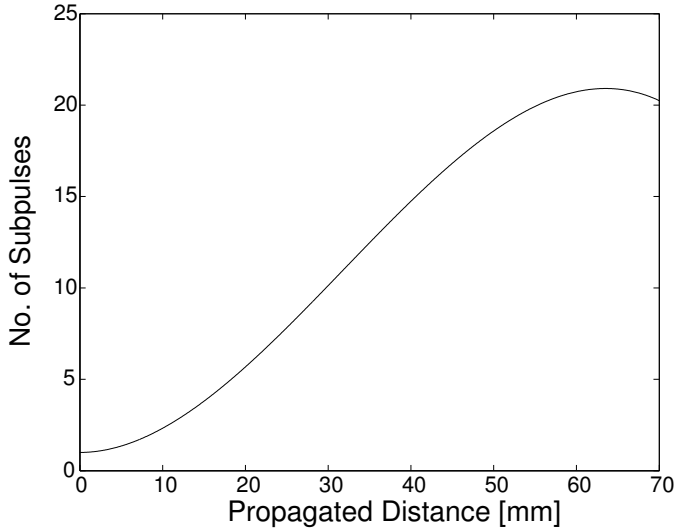

Figure 3.7: Plot showing the expected subpulse number evolution at high energy and high pressure (1.2 mJ, 130 mbar). Note the quick growth in subpulse number in the early propagation and plateau at 65-70mm propagation.

3.5 Coefficient mapping

Part of the motivation for this project is fast and efficient pump pulse and harmonic spectrum prediction. To this end, the parameters of fits, such as the $n_{sub}(z)$, $\hat{I}_n(z)$ and $\hat{T}_n(z)$ can be mapped to surfaces which predict their behaviours for any given (U, p) (pulse energy, gas pressure) to save time recalculating the parameters for every change to the setup. To this end, pump pulse simulations were run with random (U, p), keeping within $U \in [0.5, 1.2]$ mJ and $p \in [50, 140]$ mbar, and setting a minimum distance between points. At the end of each simulation, the coefficients from the fits for $\hat{I}_n(z)$, $\hat{T}_n(z)$ and $n_{sub}(z)$ were collected. These coefficient values, when plotted in (U, p) space, form

surfaces describing each parameter as a function of pulse energy and pressure. Fitting surfaces to these data then produces analytic approximations to each coefficient, which can then be combined with the fitted approximations for the other coefficients to produce analytic approximations for the intensity, width and number of subpulses as follows:

$$\hat{I}_n(z;U,p) = a_n(U,p)z^2 + b_n(U,p)z + c_n(U,p) \tag{3.5}$$

$$\hat{T}_n(z;U,p) = \exp\left(f_n(U,p)z^2 + g_n(U,p)z + h_n(U,p)\right) \tag{3.6}$$

$$n_{sub}(z;U,p) = \nu(U,p)z^3 + \tau(U,p)z^2 + 1 \tag{3.7}$$

The surfaces fitted to the coefficient values are Nth order truncated 2D Taylor series, expanded around the previously discussed "standard parameters" (section 1.5) $(U_0, p_0) = (0.8\text{ mJ}, 100\text{ mbar})$. They have the form:

$$f_N(U,p) \approx \sum_{i=1}^{N+1}\sum_{j=1}^{i} c_{i,j}(U-U_0)^{i-j}(p-p_0)^{j-1} \tag{3.8}$$

Here $\{c_{i,j}\}$ are the set of fitting parameters describing the surface, which are tabulated in appendix A. The surface is fitted by minimizing the residual sum of squares, $\sum_k [D_k - f(U_k,p_k)]^2$, where D_k is the k-th data point, and (U_k,p_k) are its corresponding pulse energy and gas pressure. This leads to the system of $(N+1)(N+2)/2$ equations which can be solved analytically by the MATLAB symbolic computing toolbox to give the set of coefficients $\{c_{i,j}\}$:

$$\sum_k \left[D_k(U_k-U_0)^{i-j}(p_k-p_0)^{j-1}\right] = \sum_k \left[f_N(U_k,p_k)(U_k-U_0)^{i-j}(p_k-p_0)^{j-1}\right] \tag{3.9}$$

With these coefficients stored, in theory, $\hat{I}_n(z;U,p)$, $\hat{T}_n(z;U,p)$ and $n_{sub}(z;U,p)$ can be quickly and efficiently calculated for any pulse energy or gas pressure within range. The surfaces describing $n_{sub}(z;U,p)$ using the aforementioned scheme are shown in figures 3.8 and 3.9.

These surfaces were calculated to 4th order with 15 coefficients apiece, the values of these coefficients are found in appendix A. Similar surfaces and coefficient tableaux were also calculated to the same order for the 15 coefficients of the $\hat{I}_1(z;U,p)$ and $\hat{T}_1(z;U,p)$ fitting constants, with the objective of doing the same for all other quantities required for construction of statistical spectra, hence removing the need to perform any pump pulse propagation simulations. However, this approach, despite decreasing statistical

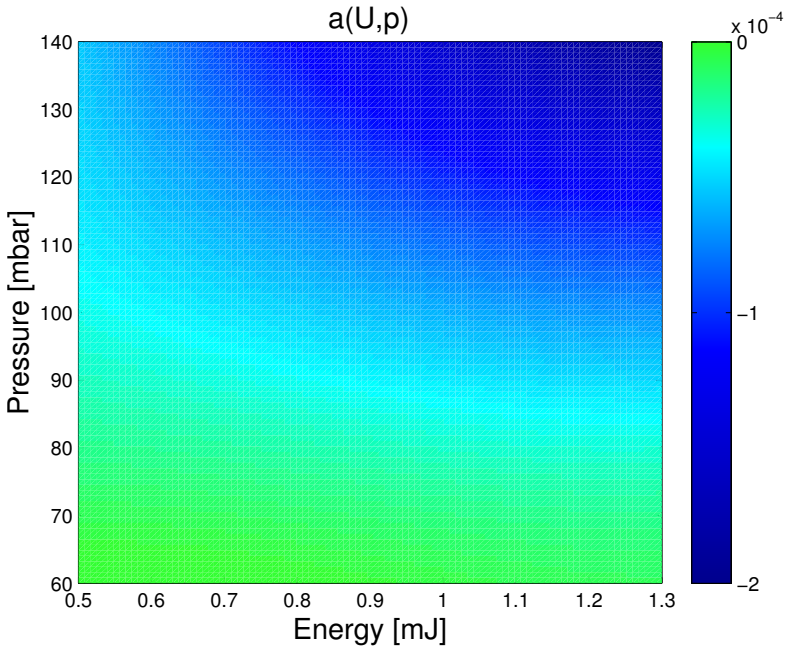

Figure 3.8: Fitted behaviour of the fitting constant a (from the fit $n_{sub}(z) \approx az^3+bz^2+1$) over an area in energy-pressure space. Note that behaviour changes are primarily driven by the gas pressure unlike most other effects in the system which are driven by the pulse energy.

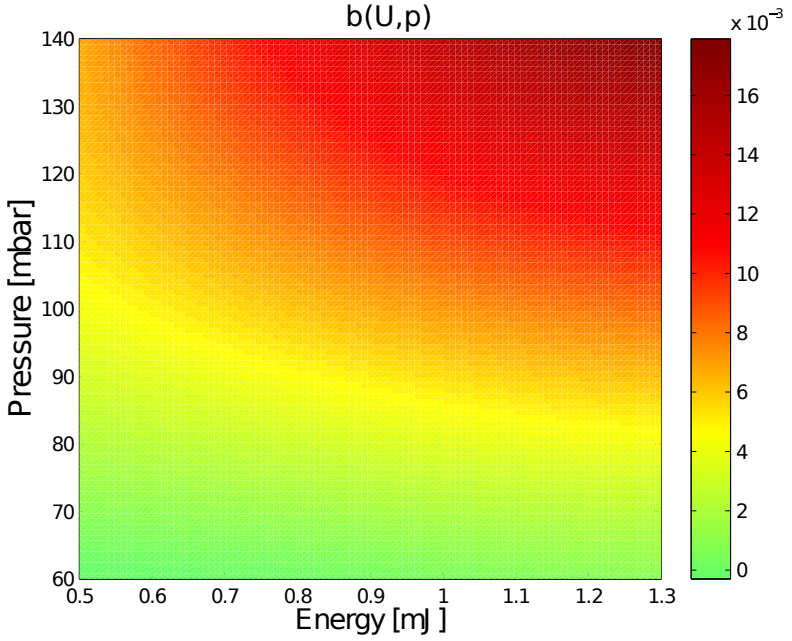

Figure 3.9: Fitted behaviour of the fitting constant b (from the fit $n_{sub}(z) \approx az^3 + bz^2 + 1$) over an area in energy-pressure space. Note the similarity in behaviour with the fitting constant a.

spectrum calculation time significantly, does not account for the high sensitivity of the pump pulse propagation on initial conditions.

3.6 Peak intensity mapping

As equation 2.11 shows, the maximum efficiently generated harmonic is a function of the peak intensity of the pump pulse. Mapping the peak intensity of the pump pulse in a similar way to section 3.5 should provide a map which indicates where the highest harmonics will be generated. As seen in figure 3.10, this peak intensity is usually found at ~ 33 mm propagation for the 75 μm radius, 7 cm long capillary. This peak comes about due to beating of the LP_{01} and LP_{02} modes, and so high intensity at this peak relies on heavy coupling into LP_{02} after the initial launch, which couples almost exclusively into LP_{01}. Such energy transfer between modes, at the gas pressures used, requires significant ionization, and hence significant intensity, to generate enough plasma response to couple energy from LP_{01} to LP_{02}, resulting in both a large ionization fraction and plenty of energy in both LP_{01} to LP_{02} to allow strong beating between those modes.

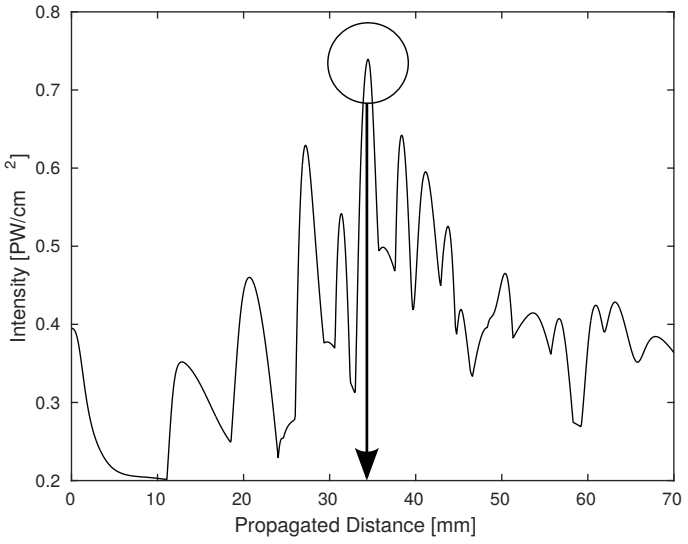

Figure 3.10: Plot of the intensity of the primary subpulse at standard parameters, as seen in figure 3.3, highlighting the persistent intensity peak at ~ 33 mm propagation.

Mapping the intensity of this peak is, however, primarily useful as a guide to finding parameter regimes in which high frequency harmonics will be produced, as opposed to a definitive guide to the specific harmonic content, since the harmonics generated at the ~ 33 mm peak have to propagate through another ~ 37 mm of argon and the highest harmonics might be subsequently highly attenuated; also, the harmonics generated at a single propagation point do not have intrinsically bright harmonics relative to the off-harmonic noise generated, so there must be some phase matching effect at a particular harmonic wavelength to produce a bright harmonic at the end of the propagation.

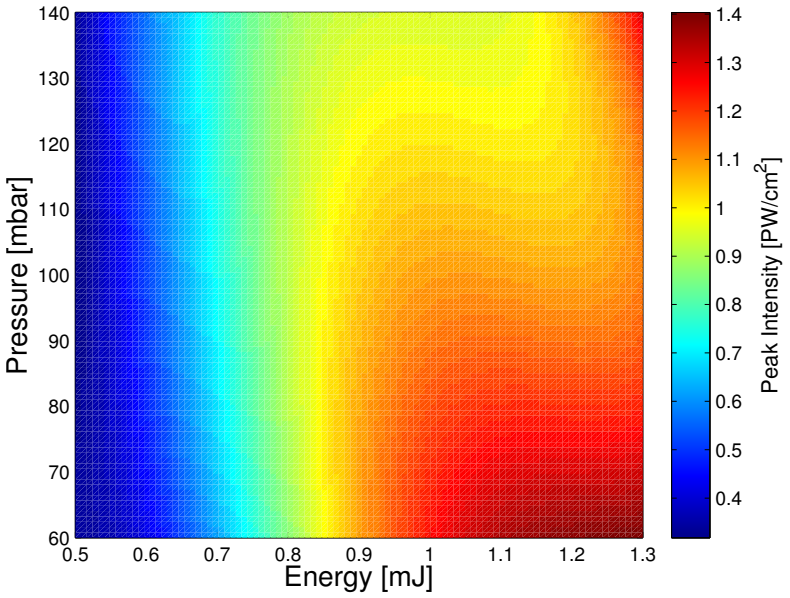

Figure 3.11: Plot of the fitted behaviour of the 33mm intensity peak height, as shown in figure 3.3 over an area in energy-pressure space. Note the low intensities at all low energies, and the particularly high intensity in the high energy, low pressure regime.

Figure 3.11 shows the peak intensity of the propagating pulse for $(U, p) \in$ ([0.5,1.3] mJ, [60,140] mbar), fitted to a 2D 4th order truncated Taylor series, as in section 3.5. As expected, low pulse energy results in universally low intensity peaks, this is because the plasma nonlinearities which result in coupling from LP_{01} to higher order modes, and hence the buildup of intensity at $\sim$ 33 mm, are barely excited, especially at low pressures.

In the high pulse energy region there is significant buildup of intensity at $\sim$ 33 mm. This is due to the extreme levels of ionization seen at such high initial pulse intensities causing almost universal ionization, which produces very high levels of plasma defocusing which allows for excitation of higher order modes, but also causes high levels of plasma absorption, resulting in significant attenuation. This balance of plasma effects is very prominent in the high pulse energy region of figure 3.11. Here the losses at high pressures are not compensated for by the additional coupling into higher order modes, resulting in lower peak intensities for such regimes. In the high energy, low pressure regime, however, the loss of extra coupling into higher order modes is more than compensated by the reduced attenuation by the generated plasma, resulting in very high peak intensities. The main drawback of operating in this regime, however, is that the lack of gas pressure results in fewer harmonic photons being generated, and although the higher pump pulse intensities will cause higher order harmonics to be generated, the overall flux of the harmonics will suffer as a result of fewer generating atoms.

3.7 Statistics of fast fluctuations

As discussed in section 3.3, the fast fluctuations describe the intensity and width behaviour of the pump pulse's subpulses, outside of the long-distance slow fluctuations. Their behaviours display two properties which make them bad targets for curve fitting: the intensities and widths change over very small distances, and also vary quite erratically. With this knowledge, a statistical description seems much more apt, and given that the fast fluctuations are normalised to unity over the propagation, fluctuations from different regions of the propagation can be compared without weighting, allowing the statistics of intensity and width fluctuations to be calculated over the whole propagation.

Finding a distribution for such quantities is nontrivial, although there are several requirements for a suitable distribution:

- Semi-finite or finite support: There are no negative intensities or widths, and so a distribution should reflect this and have zero probability for any negative intensities or widths; this discounts some usual distributions like the Gaussian. There is no theoretical limit on how intense or wide an outlier subpulse may be so a potential distribution should reflect this and allow for such high intensities and widths even if that probability is very small, which indicates that semi-finite support would be prudent, although a distribution with finite support can potentially provide a good approximation.

- Simplicity: Although almost any space or distribution can be well approximated by an N-D truncated Taylor series, the number of coefficients required to define the surface quickly becomes restrictive as the order of the approximation grows, and so for particularly nontrivial spaces and distributions, such methods become unviable. An ideal distribution is one which can approximate the statistics of the underlying data accurately enough to recover the basic statistics while requiring as few coefficients as possible.

- Covariance: Although the subpulse intensities and widths have been considered seperately thusfar, and for a significant proportion of this section, energy conservation indicates that in the ideal case $I_n T_n \approx$ const. (the quantities are inversely propotional to each other) and so there should be some level of covariance between the intensities and widths (since the energy in a Gaussian pulse $\propto IT$), as shown in figure 3.12. This assumes there is little energy transfer between subpulses, which is the ideal case for the subpulse decomposition. Although this ideal case does not exist, the normalized covariance between $\tilde{I}$ and $\tilde{T}$ gives an indication of how well the subpulse model applies, and an appropriate distribution of $\tilde{I}$ and $\tilde{T}$ should reflect this by including the covariance between the two parameters. This criterion is expanded upon in section 3.8.

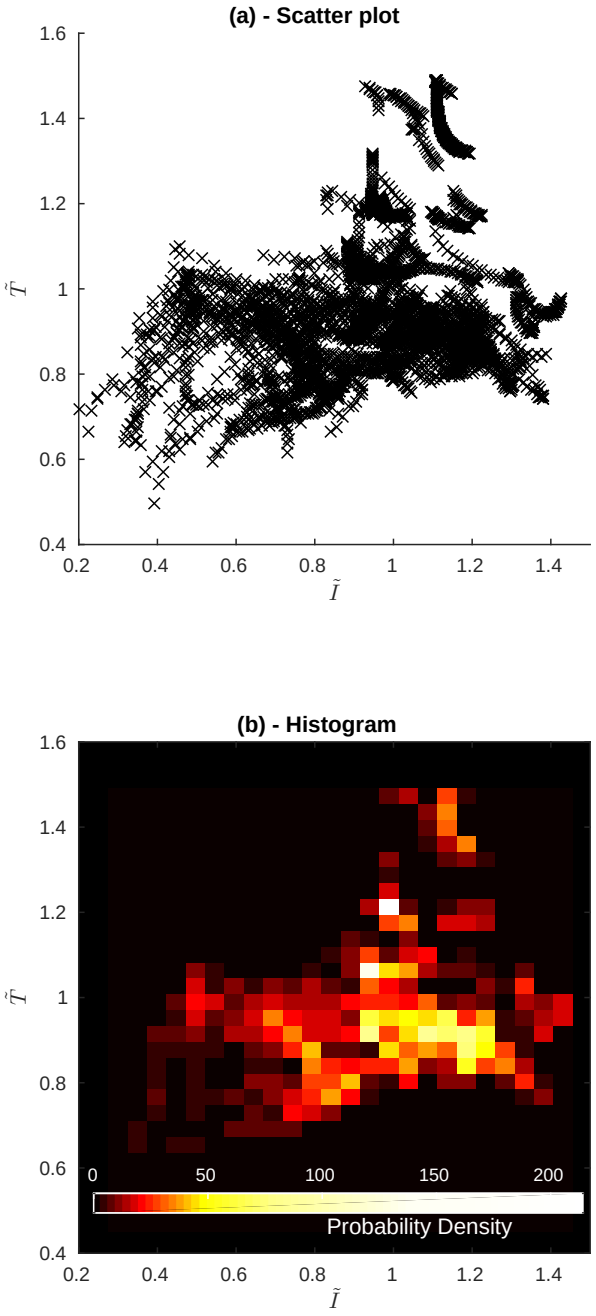

Figure 3.12: (a) A scatter plot of $\tilde{I}$ and $\tilde{T}$ for a pulse propagating with "standard" energy and pressure, including all subpulses. Note the large gaps separating parts of the distribution at high $\tilde{T}$.
(b) Histogram of the above scatter, showing more clearly the smoother distribution around (1,0.9) and the isolated probability peaks at high $\tilde{I}$ and $\tilde{T}$.

As a first approximation, the covariance can be ignored to allow the use of two 1D distributions. The first two criteria still apply, and in this vein, a gamma distribution was chosen of the form:

$$\gamma(x, k, \theta) = \frac{x^{k-1} e^{-x/\theta}}{\theta^k \Gamma(k)}$$

here k is the shape parameter and θ is the scale parameter, both of which define the shape of the distribution and serve as fitting constants. A third parameter, m can also be introduced in $x \to x - m$ which allows for shifting of the mean, resulting in increased flexibility and hence improved fitting. With only 3 free parameters, this distribution fulfils the simplicity criterion. The function is also only valid for $x > m$ which also satisfies the semi-finite support criterion, and to a good approximation, the support can be roughly finite.

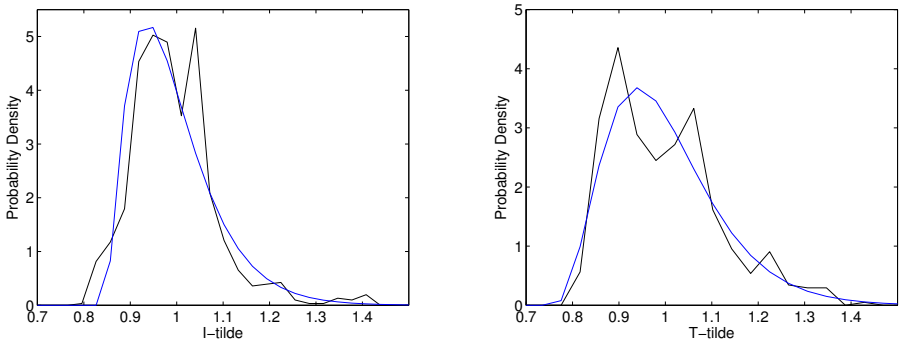

Figure 3.13: Plots of the $\tilde{I}_1$ and $\tilde{T}_1$ histograms, with shifted gamma distribution fits, using the data from the primary subpulse at standard parameters. Note the similarity in shape, particularly noting the sharp cutoff at, and skew towards, low $\tilde{I}$ and $\tilde{T}$, as well as the exponential tailoff towards high values.

Such curves can be easily fitted to the 1D histograms of $\tilde{I}$ and $\tilde{T}$, as shown in figure 3.13. These fits provide good approximations to the histogram data and recreate many features seen in the distributions such as the sharp cutoff at low values and tailoff at high values. There is also strong skew in both distributions, and, as figure 3.13 shows, the γ distribution is well equipped to deal with this, although the fit is not accurate for negatively skewed data as the γ distribution can only have positive skew. To remedy this, the data must be flipped about the mean to produce an apparent positive skew; after fitting, the fitted distribution can then be flipped about the mean to produce a gamma distribution with negative skew, although since $\tilde{I}, \tilde{T} > 0$, the fitted distribution must satisfy $\gamma(x \to 0) \to 0$ which is usually well adhered to.

3.8 Covariance of subpulse intensities and widths

As mentioned in section 3.7, there is a great deal of covariance between $\tilde{I}$ and $\tilde{T}$. It was also noted that due to energy conservation concerns, the level of covariance between the two quantities provides some insight into the energy conservation between subpulses and the overall applicability of the description.

To evaluate the covariance between the intensities and widths, a normalised covariance, the Pearson coefficient, $\rho(x,y) = \frac{\mathrm{cov}(x,y)}{\sigma_x \sigma_y}$, is used. This coefficient allows the covariance of pump pulse propagations with a wide range of starting conditions to be compared on an equal footing to find system parameter regimes where the algorithm applies particularly well. These data are given in figure 3.14.

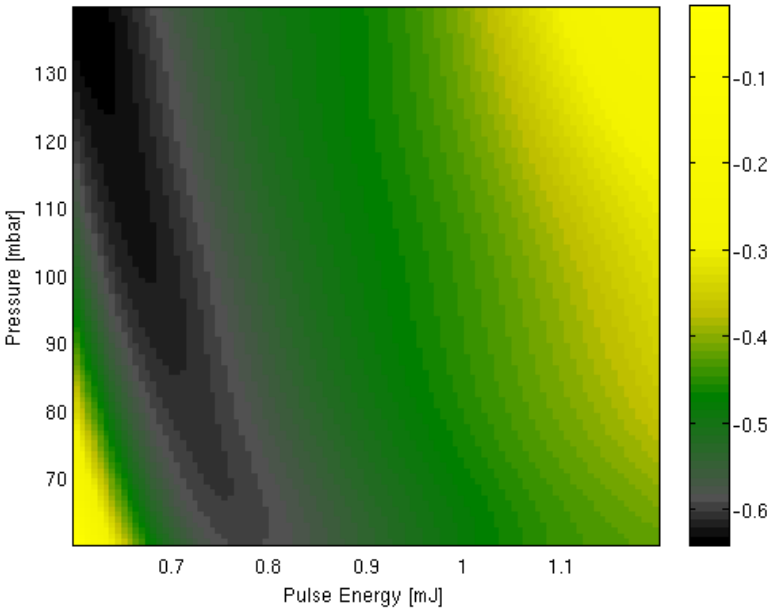

Figure 3.14: Plot of the Pearson correlation coefficient between the width and intensity of the primary subpulse, for a range of pulse energies and gas pressures. Note the high degree of negative correlation along the line (0.8,60) → (0.6,130) and the lack of correlation at (0.6,60) and (1.2,140).

As figure 3.14 shows, there is significant correlation between $\tilde{I}$ and $\tilde{T}$ across the parameter space, especially around the 0.8 mJ 100 mbar standard parameter region, with Pearson coefficients approaching -0.6. The ideal case is one where $\rho \to -1$, so $\rho = -0.6$ indicates a strong level of correlation between $\tilde{I}$ and $\tilde{T}$. Strong correlation indicates that there is no energy transfer between subpulses as they propagate and that they are hence almost entirely autonomous, which is one of the basic assumptions for the approach to pulse deconstruction. This level of correlation around the standard parameters provides strong justification for using a bivariate distribution despite the extra difficulty in defining and fitting the distribution as opposed to two 1D distributions.

3.9 Joint statistics of fast fluctuations

The primary problem with the 1D distributions of section 3.7 is that they do not account for the 3rd aforementioned criterion: covariance. As previously mentioned, it is very important that any distribution of $\tilde{I}$ and $\tilde{T}$ contain the covariance between them; it is also preferable to stick with a distribution which has shown many of the features desired from an ideal distribution, such as the above 1D γ distributions. There is no simple method of deriving a 2D equivalent of the 1D γ distributions which includes covariance, although through some very technical mathematics, the following was derived by [46]:

$$\begin{aligned} PDF(x,y;k_1,k_2,\theta_1,\theta_2,m_1,m_2,\rho) = \\ \gamma_1(x;k_1,\theta_1,m_1)\gamma_2(y;k_2,\theta_2,m_2)\frac{1}{\sqrt{1-\rho^2}} \times \dots \\ \cdots \times \exp\left[-\frac{1}{2(1-\rho^2)}\left[[\rho\Phi^{-1}(F(x;k_1,\theta_1,m_1))]^2 - \dots\right.\right. \\ \cdots - 2\rho\Phi^{-1}(F(x;k_1,\theta_1,m_1))\Phi^{-1}(F(y;k_2,\theta_2,m_2)) + \dots \\ \left.\left. \cdots + [\rho\Phi^{-1}(F(y;k_2,\theta_2,m_2))]^2\right]\right] \end{aligned} \tag{3.10}$$

$$F(x;k,\theta,m) = 1 - \frac{\Gamma(k,x/m)}{\Gamma(k)}$$

$$\Phi^{-1}(F(x;k,\theta,m)) = \sqrt{2}\,\mathrm{erf}^{-1}(2F(x;k,\theta,m)-1)$$

Here $\gamma_1(a;b,c,d)$ is the 1D gamma distribution of a with shape b, scale c and abscissal offset d, $\Gamma(a,b)$ is the upper incomplete gamma function of a, starting at b; $\Gamma(a)$ is the complete gamma function of a [47]; ρ is the Pearson correlation coefficient; and $\mathrm{erf}^{-1}(a)$ is the inverse error function of a.

Fitting such a function to data such as that in figure 3.12 is a nontrivial task, since a least squares fit to such sparse data results in a lot of locally minimal solutions, the majority of which are extremely poor fits which display few of the features of the raw data. To circumvent this highly nontrivial global optimization problem, the distribution is fitted by an alternate method: a statistical fitting. This fitting method works similarly to least squares, but instead of fitting to the data the distribution's statistics are fitted to those of the data. This is done by generating equation 3.10 for arbitrary coefficients (ρ is set and fixed by direct calculation) and calculating the means, $\langle I\rangle_\Gamma$ & $\langle T\rangle_\Gamma$, the variances, $\sigma_{\Gamma I}$ & $\sigma_{\Gamma T}$, and the skews, $S_{\Gamma I}$ & $S_{\Gamma T}$ of the distribution. These are then compared with the equivalent quantities from the data: $\langle I\rangle_D$ & $\langle T\rangle_D$, σ_{DI} & σ_{DT}, and S_{DI} & S_{DT}. The

statistics from both distribution and data are then compared, normalised, and summed to form a cost function:

$$
\begin{aligned}
L \;=\; & \frac{|\langle I\rangle_D - \langle I\rangle_\Gamma|^2}{|\langle I\rangle_D + \langle I\rangle_\Gamma|^2} + \frac{|\langle T\rangle_D - \langle T\rangle_\Gamma|^2}{|\langle T\rangle_D + \langle T\rangle_\Gamma|^2} + \\
& \frac{|S_{DI} - S_{\Gamma I}|^2}{|S_{DI} + S_{\Gamma I}|^2} + \frac{|S_{DT} - S_{\Gamma T}|^2}{|S_{DT} + S_{\Gamma T}|^2} + \\
& \frac{|\sigma_{DI} - \sigma_{\Gamma I}|^2}{|\sigma_{DI} + \sigma_{\Gamma I}|^2} + \frac{|\sigma_{DT} - \sigma_{\Gamma T}|^2}{|\sigma_{DT} + \sigma_{\Gamma T}|^2}
\end{aligned}
$$

This cost function is then minimized by MATLAB's optimization toolbox functions, giving the set of constants $\{k_1, k_2, \theta_1, \theta_2, m_1, m_2\}$ which define the fitted bivariate gamma distribution.

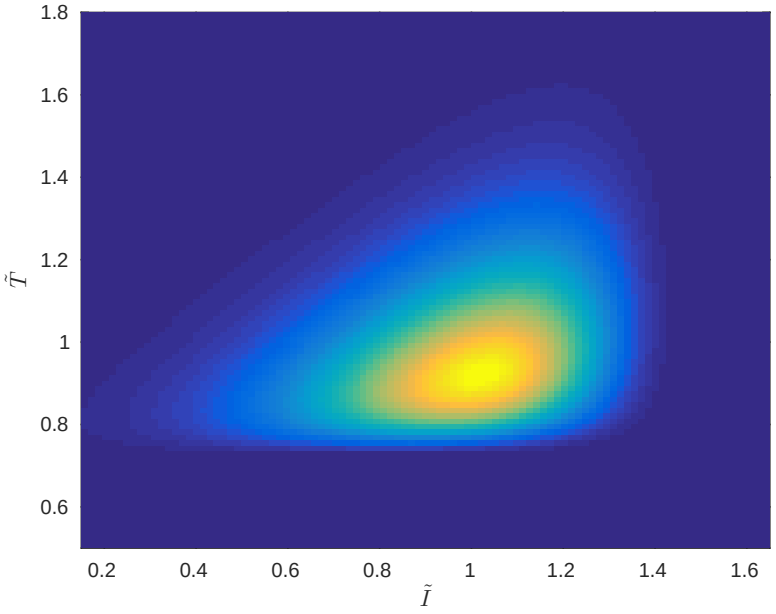

Figure 3.15: The gamma distribution ($\kappa_I = 7.0976, \kappa_T = 2.9801, \theta_I = 0.0825, \theta_T = 0.0949$) corresponding to the $\tilde{I}$ and $\tilde{T}$ data collected for the entire subpulse ensemble at "standard parameters". Note the peak at (1,0.996) and the sharp cutoffs at lower $\tilde{I}$ and $\tilde{T}$, the strong covariance at high $\tilde{I}$ and $\tilde{T}$.

As figure 3.15 shows, the bivariate covariant γ distribution fits the distribution indicated by the histogram (figure 3.12(a)) quite well, successfully encapsulating the main features seen in the data.

3.10 Analysis of fitting and mapping

The biggest fitting challenge in this work, and the fitting which has the biggest impact on the subsequent calculation of HHG spectra, is the bivariate gamma distribution fitting described in section 3.9. Good fitting, representative of the underlying data, is required here to take into account the pump pulse behaviours, and a failure to describe the distribution of the underlying data would reduce the reliability of the simulated HHG spectra.

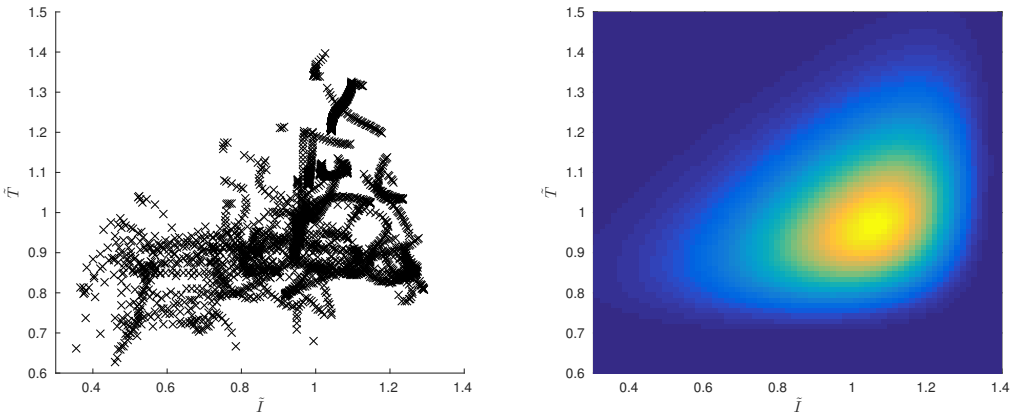

Figure 3.16: The scatter of $\tilde{I}$ and $\tilde{T}$ at 0.7 mJ, 90 mbar, showing the similarity in the distributions of data and fit.

As figure 3.16 shows, the statistical fitting is both visually successful and provides a very close match between the statistics of the data and distribution:

	$\langle I \rangle$	$\langle T \rangle$	σ_I	σ_T	S_I	S_T
Data	1.0395	0.96493	0.19241	0.14208	0.77027	0.71706
Distribution	1.0408	0.96477	0.19241	0.14208	0.77027	0.71706

As the above table shows, the statistics of the data and bivariate γ distribution are well matched; given that the distribution is also a visually good fit, this gives credibility to the bivariate gamma distribution as a good representation of the distribution of $\tilde{I}$ and $\tilde{T}$. Although obviously the data to which the distribution is fitted is sparse, the statistics of the data are unlikely to be particularly different for a statistically large number of data points, given the shape of the distribution is often well defined. Adding more points to the propagation increases the number of ($\tilde{I}$,$\tilde{T}$) data available for fitting, although this behaves like an interpolation, simply tracing paths between the existing points, which has a negligible effect on the statistics.

Chapter 4

Statistical Spectra and Analysis

The final construction of the "statistical" high harmonic spectra requires the following information:

- Precalculated single-atom spectra, calculated using the semi-classical model of section 2.2.3, which describe the HHG spectra generated by Gaussian pulses of all intensities and FWHMs encountered in the pump pulse propagation.
  - Because typical subpulse intensity profile shapes can be well approximated by Gaussians, an array of Gaussian pulses of different widths and intensities essentially forms an idealised set of all possible subpulses and hence the spectra generated from such pulses form a set of all the possible HHG spectra that can be generated by the subpulses in the pump pulse propagation. These Gaussian pulses are assumed to have zero carrier-envelope-phase, since the phase information from the pump pulse propagation has already been discarded to limit the amount of data to a practical amount.
  - For practical purposes, the range of subpulse intensities and FWHMs for which these spectra are calculated is limited by the maximum intensities and widths seen, although for flexibility and convenience these maxima are extended past the observed maxima. Minima are also imposed on the intensity and FWHM considered, these are more limits imposed by the methods used, with a minimum intensity (as described in section 3.2) where the semi-classical model used fails and only uninteresting harmonics are generated; and a near single-cycle pulse minimum FWHM, in which a generated spectrum depends significantly on the carrier-envelope-phase, which is not considered. Explicitly, the range of intensities and FWHMs considered are hence $I \in [0.01, 1.28]$ PW/cm^2 and $T \in [3, 66.5]$ fs.
- The averaged slow subpulse fluctuations $\hat{I}_m(z)$ and $\hat{T}_m(z)$ corresponding to the averaged $I(z)$ and $T(z)$ (using the methods described in section 3.4) and their

corresponding fast fluctuations $\tilde{I}_m(z)$ and $\tilde{T}_m(z)$ which are calculated from the same averaged intensity and width profiles.

  - The fast and slow fluctuations derived from the averaged intensity and width evolutions are used here because, as section 3.7 describes, the bivariate gamma distribution is calculated from the intensity and FWHM propagation of the ensemble of all subpulses. This means that the slow fluctuations that are used in the statistical spectrum construction should be representative of all subpulses.

- $n_{sub}(z)$ and pressure profile.
  - Since $\hat{I}_m(z)$ and $\hat{T}_m(z)$, by which $\tilde{I}_m$ and $\tilde{T}_m$ are normalized, are calculated from intensity and FWHM evolutions which are averaged over all subpulses, any spectra "generated" at a particular z must be scaled by the number of subpulses at that point, although the fitted $n_{sub}(z)$ calculated in section 3.4 is used over the explicitly measured number of subpulses to average-out the occasional artefact-subpulses which occasionally appear briefly due to pump pulse shapes that are mishandled by the subpulse finding algorithm.
  - The pressure profile has a very similar effect, since the precalculated spectra are single-atom, the spectra "generated" at a given z must be scaled by the number of atoms at that point, although since the units of the intensity profile of the statistical spectra are unknown, they are normalized to the highest intensity seen between 20 and 35 nm wavelength, and so the pressure in mbar, or any other unit of pressure is as good a scaling factor as the number of atoms.

- Other required data include the bivariate gamma distribution describing the intensities and FWHMs of all subpulses, as described in section 3.7.

With these data ready, the statistical spectra can be calculated using the following algorithm. For each intensity, I_n, and FWHM, T_n, considered:

1. Effective $\tilde{I}$ and $\tilde{T}$ values for an entire propagation are calculated by taking $\sqrt[3]{I_n/\hat{I}_m(z)}$ and $\sqrt[3]{T_n/\hat{T}_m(z)}$, which can then be used with the bivariate gamma distribution to produce a weight function for the current (I_n, T_n): $W_n(z)$.

2. $W(z)$ is then scaled by the pressure and number of subpulses according to $W(z) = W_n(z) \times n_{sub}(z) \times p(z)$, where $p(z)$ is the pressure profile along z

3. The contribution to the statistical spectra from the current (I_n, T_n) is then given by:

$$\tilde{E}_h(\omega, z) = \sum_n W(z) \exp[\tilde{\alpha}(\omega)(z - z_{max})/2]\omega dz P_n^{dip}(\omega)$$

where $P_n^{dip}(\omega)$ is the precalculated HHG spectrum corresponding to (I_n, T_n).

When the above algorithm is repeated for each (I_n, T_n) combination, the statistical spectra can be calculated in two ways: firstly the coherent spectrum, which accounts for the phase of the harmonic spectrum, is given by $\tilde{I}_{coh}(\omega) = |\sum_z \tilde{E}_h(\omega, z)|^2$ and the incoherent spectrum, which disregards the phase of the harmonic spectrum, given by: $\tilde{I}_{inc}(\omega) = \sum_z |\tilde{E}_h(\omega, z)|^2$.

Note that the coherent statistical spectrum can be "hand phase matched" (phase shifted uniformly at each z to give a certain frequency constant phase along the propagation), along the propagation to a specific frequency, ω_{pm} by taking:

$$\tilde{I}_{coh}(\omega) = |\sum_z \tilde{E}_h(\omega, z) e^{-i\Phi(\tilde{E}_h(\omega_{pm}, z))}|^2 \tag{4.1}$$

where $\Phi(\tilde{E}_h(\omega_{pm}, z)$ is the phase of the harmonic field at the phase-matched frequency ω_{pm}, providing a useful tool for investigating the phase matching in the generated harmonic field, as will be discussed in section 4.3.

4.1 Computational efficiency of the statistical spectra

The process of calculating statistical spectra is markedly quicker than that of performing full simulations, given that the limiting step is incorporation of the absorption of the XUV. The time for an explicit semi-classical simulation given a precalculated pump pulse propagation is $\sim$ 15 hours, whereas for a statistical spectrum, the simulation can be complete in $\sim$ 7.5 mins (on a 3.4GHz Intel i7-3770 CPU) which is less than the $\sim$ 8.5 min pump pulse propagation time. Assuming that the precalculated spectra are in an easily accessible storage device, and ignoring the pump pulse propagation simulation which both methods require, the statistical method provides a $\sim$ 57x speed improvement over the explicit semi-classical simulations. The time efficiency of the first few statistical spectra is somewhat hampered by the several days it takes to precalculate the spectra corresponding to the Gaussian pulses of variable width and intensity, although because of the significant difference in simulating times, the statistical method becomes significantly more time efficient after 4 simulations, allowing for rapid mass-simulation.

4.2 Analysis of statistical and explicit spectra

The statistical spectra (figures 4.1 and 4.2) show the classic harmonic structure, as seen in the explicit spectrum in figure 4.3; this is expected since there is no fundamental difference in how single-atom spectra are integrated together over the course of the

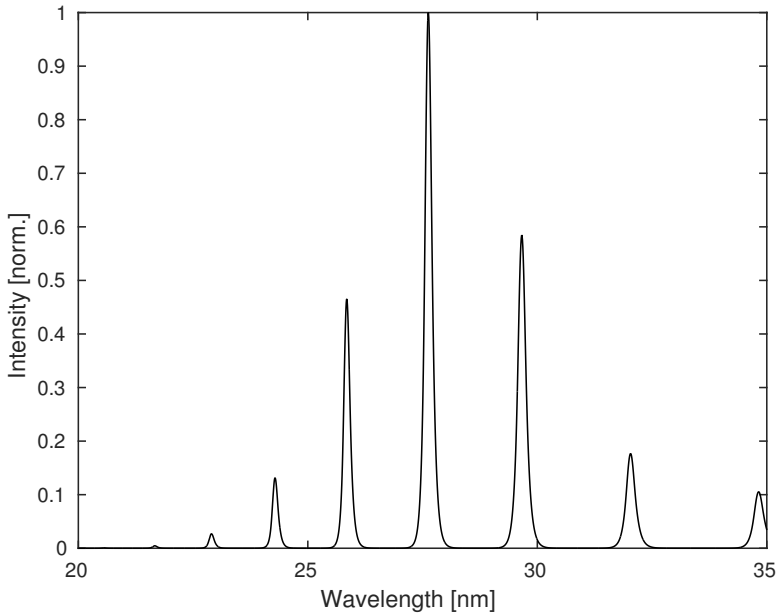

Figure 4.1: Figure showing the coherently integrated statistical spectrum in the $\lambda \in [20, 35]$ nm range, generated from a pump pulse at "standard parameters" (0.8 mJ, 100 mbar). Note the sharp, distinct, harmonics and lack of noise floor.

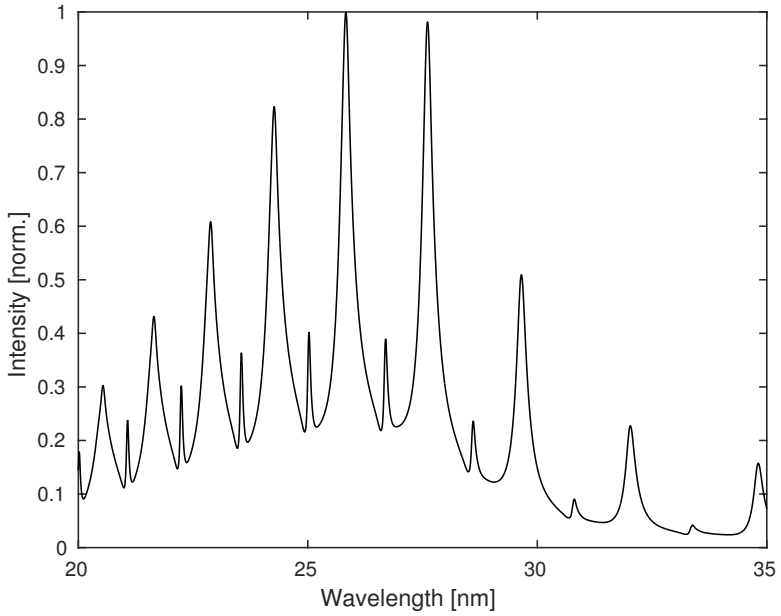

Figure 4.2: Figure showing the incoherently integrated statistical spectrum generated from a pump pulse at "standard parameters" (0.8 mJ, 100 mbar). Note the high noise floor and small even harmonics.

propagation, although as section 4.3 discusses, the differences in phase matching may lead to other differences in the spectrum structure.

The harmonic envelope is quite well predicted by the statistical spectra, with only one

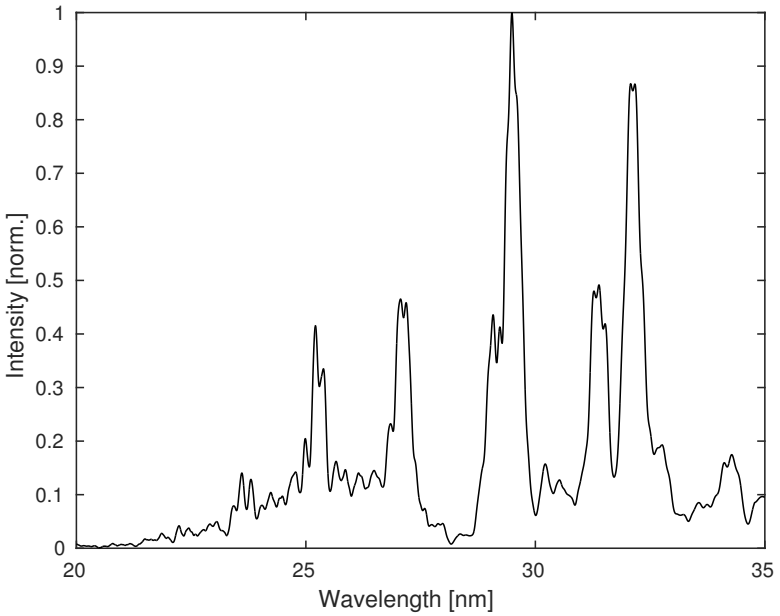

Figure 4.3: Figure showing the explicitily simulated HHG spectrum for "standard parameters", smoothed to 1 eV resolution. It highlights the nontrivial structure of the generated spectra and the sharp peaks, as well as the off-harmonic components generated by the large pump pulse bandwidth.

odd harmonic difference in the peak of the envelope between the statistical and explicit spectra. Although this envelope is partly set by the argon absorption spectrum (figure 2.11), there are some features of the spectra which indicate coherent buildup of harmonics above the off-harmonic regions and argon absorption. Pure shaping by the argon absorption spectrum would cause a sharp drop in intensity of the 29.6nm harmonic and longer wavelengths whereas the intensity drop seen at these wavelengths in the statistical spectra is relatively gentle, indicating the presence of a wavelength-dependent build up mechanic. Similarly, the relatively sharp intensity drop-off seen at short wavelengths relative to the argon absorption spectrum indicates that this is shaped by a process other than gas absorption.

In the coherently-integrated spectrum, figure 4.1, the noise is almost entirely eliminated due to the random phases found therein averaging to zero, whereas in the incoherent spectrum (figure 4.2), the intensities of the noise components are integrated together, and since they are necessarily > 0, the noise floor is consistently high.

The coherently integrated spectrum shows the lack of even harmonics seen in the explicitly simulated spectra (those simulated directly from the pump pulse using the theory of section 2.2.3) and expected from the theory laid out in section 2.2.2, although the incoherently integrated spectrum, appears to show indications of even harmonics above its noise floor, which is again due to the addition of intensities as opposed to the addition of complex fields in the harmonic field buildup over the propagation.

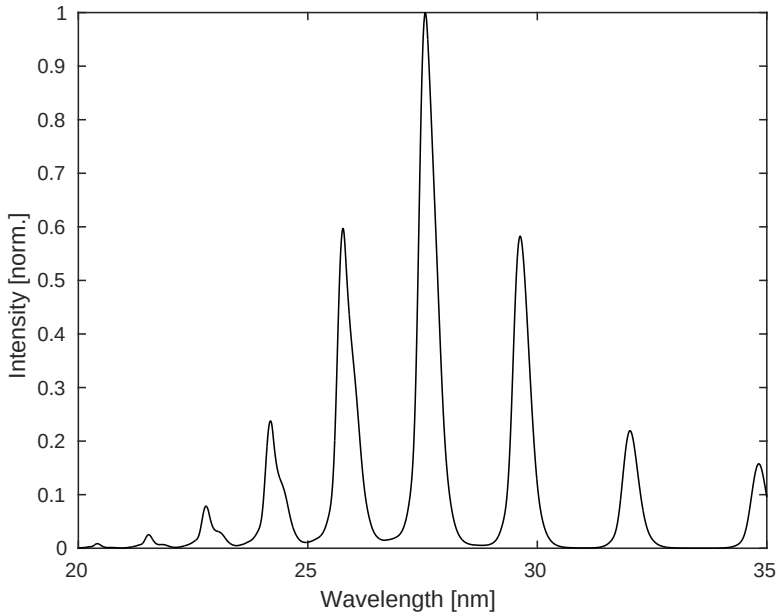

Figure 4.4: Figure showing the coherently integrated statistical spectrum generated from a pump pulse at 1.2 mJ, 100 mbar. Note the wider harmonics and envelope shift to shorter wavelengths compared to figure 4.1

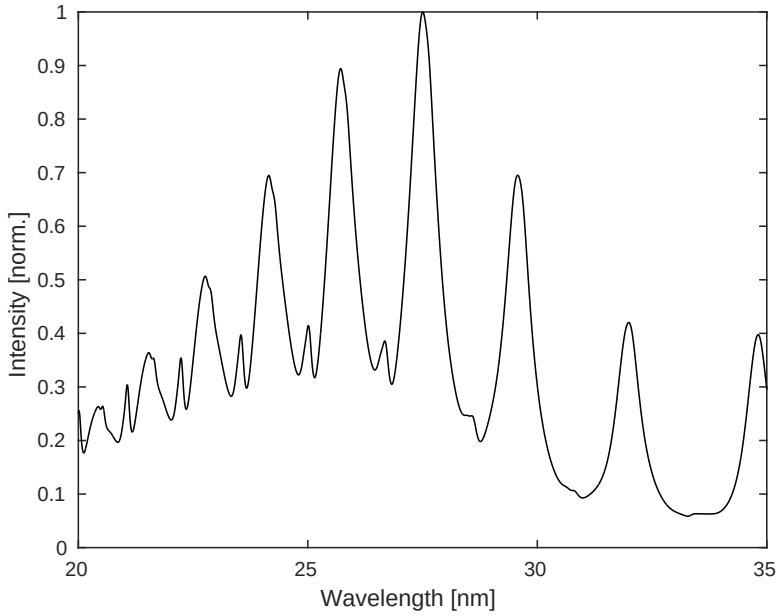

Figure 4.5: Figure showing the incoherently integrated statistical spectrum generated from a pump pulse at 1.2 mJ, 100 mbar. Note the wider harmonics and envelope shift to shorter wavelengths compared to figure 4.2, as well as the suppression of the ideally disallowed even harmonics.

The statistical spectra at 1.2mJ, 100 mbar (figures 4.4 and 4.5) show a lot of the key features seen at standard parameters. Firstly the coherent spectrum looks very similar,

with the same basic structure and similar envelope. The most glaring difference is that in the high energy case the harmonic envelope is shifted towards shorter wavelengths, with those harmonics accumulating more energy due to the increased generation of short wavelengths from the higher intensity pump pulse. This shift towards higher frequencies is also seen when comparing the explicitly simulated spectra, figures 4.3 and 4.6, with significantly more energy overall going into short wavelengths in the 1.2 mJ case while still retaining the peak at 29.6nm.

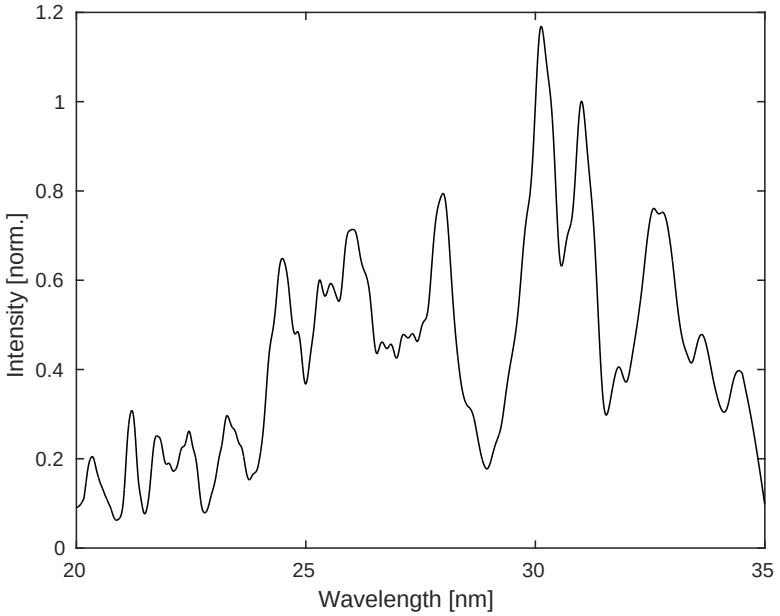

Figure 4.6: Explicitly simulated harmonic spectrum generated at 1.2mJ, 100 mbar. Note the high noise floor and poorly defined harmonics compared to figure 4.3, and the bright non-harmonic peaks generated by the broad bandwidth of the pump pulse.

Another effect of higher pulse intensity seen in the explicit simulations is the widening of harmonics due to an absolute increase in the intensity of frequencies far from the central frequency, giving rise to harmonics with slightly shifted wavelengths which cumulatively manifest themselves as wider wings on each harmonic. This effect is seen quite clearly in the statistical spectra, with both coherently and incoherently integrated spectra showing the widening.

4.3 "Hand phase matching" and discussion of phase matching in statistical spectra

As previously mentioned, phase matching is a crucial element of harmonic build-up, ensuring that the odd harmonic frequencies grow, while the noise in between them is suppressed. Since this is neglected in the statistical spectra, the statistical spectra

struggle to have their envelopes peaking at the 25th and 27th harmonics as seen in the explicitly simulated spectra. Instead, the statistical spectra tend to peak around the 29th harmonic because this is where the argon absorption is at its minimum.

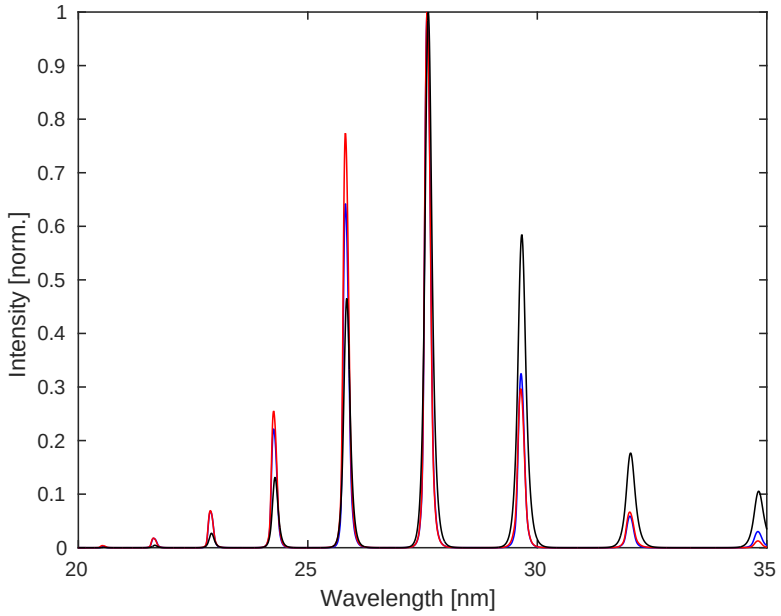

Figure 4.7: Statistical spectra at "standard parameters", as in figure 4.1, unmodified (–), and hand phase matched to the 29th (–) and 27th (–) harmonics, respectively.

Figure 4.7 shows the statistical spectrum at standard parameters (figure 4.1), except the single-atom spectra at each propagation step are phase-shifted to either the 27th or 29th harmonic, "hand phase-matching" that harmonic along the propagation, as discussed in section 4. These spectra show an improvement in envelope peak position when compared to the explicit spectrum (figure 4.2), which is expected, since the phase-matched harmonics should grow disproportionately over the course of the propagation. Surprisingly, however, the phase matched harmonics are not the harmonics with the greatest intensity, although given that all the harmonics in the region are fairly well phase matched anyway, the effect of hand phase matching seems to be heavily diminished, and only manifest itself as a shift towards the chosen harmonic. This also indicates that the phase matching conditions in the explicit spectra have very localised regions of good phase matching, since the bright harmonics in the explicit spectra are disproportionately brighter than their surroundings indicating poor phase matching in the off-peak regions.

4.4 Power/pressure scaling

A potential prediction of the statistical spectra is the scaling of the total energy in the harmonic spectrum in the region of interest. Since experimentally this region or an

analogous region would be transmitted more readily than other wavelengths, analysing how the energy of the harmonics in this region scales will give an indication of how the flux of the experimental system would vary with changing pulse energy and gas pressure.

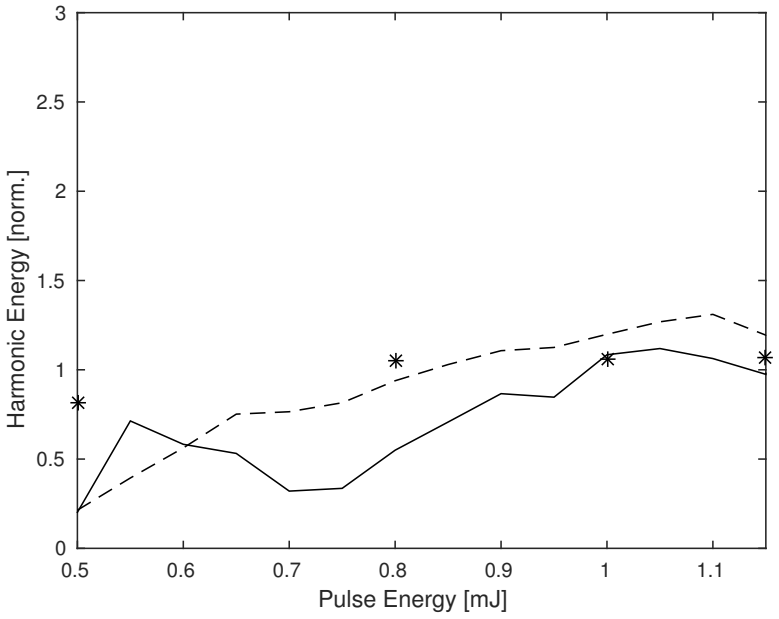

Figure 4.8: Normalized energy of the statistical spectra in the wavelength range $\lambda \in [20, 35]$ nm, for coherently (–) and incoherently (- -) integrated spectra generated from pulse propagations with 100 mbar pressure and $U \in [0.5, 1.15]$ mJ energy. Discrete energies for explicitly simulated spectra (*) provided for comparison. Note the similarity between the explicitly simulated data and incoherently integrated spectra.

Figure 4.8 shows how the energy of the 20-35 nm harmonics of the statistical spectra vary with changing pulse energy, respectively. The behaviours are shown for three cases: explicit simulation (*), coherently integrated statistical spectra (–) and incoherently integrated spectra (- -), each normalised to their mean to remove arbitrary scaling factors.

The scaling of the 20-35nm harmonic energy, as calculated by the statistical method, with pulse energy shows correlation with the explicitly simulated spectra, although not perfect, it does capture the overall trend, which is testament to the integrity of the $\tilde{I} - \tilde{T}$ distribution and the weighting it gives the ensemble of single-atom spectra. The incoherently integrated spectrum follows the explicitly simulated energy scaling behaviour more closely than the coherently integrated spectrum. This is because the nonlinear phase profile of the pump pulse and subsequently highly nontrivial phase matching conditions of the harmonics are not sufficiently compensated for by the phase matching used in the coherently integrated spectra.

Scaling of the 20-35nm harmonic energy for constant pulse energy and variable gas pressure does not follow the corresponding behaviour of the explicitly simulated spectra,

because the gas pressure prescribes phase matching lengths which the statistical model then ignores, and hence the statistical model is unable to account for the changes in phase matching which occur with variable pressure. This means that the total harmonic for a range of pressures is usually either under- or over- phase matched, and hence the overall scaling trend does not fit with corresponding data generated through explicit simulation.

4.5 Harmonic Width

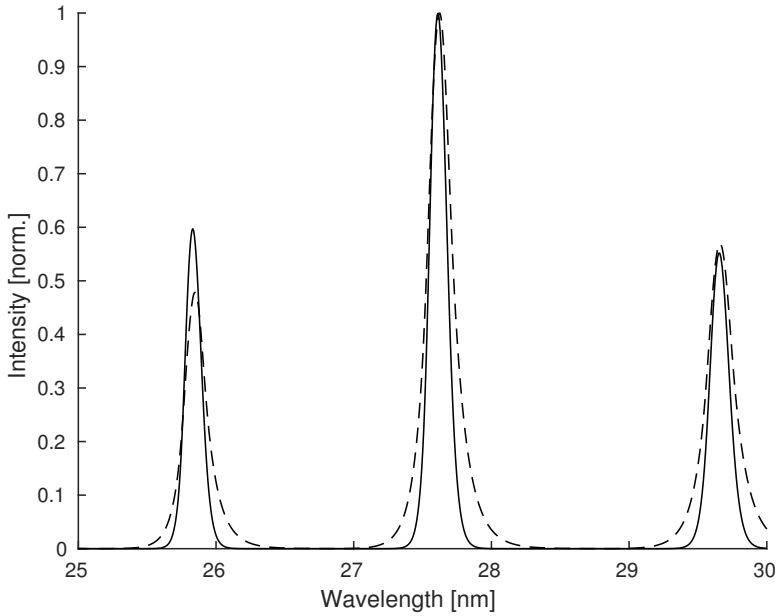

Figure 4.9: Plot showing the statistical spectra generated from a pump pulse of 0.8 mJ and 60 mbar (–), and from a pump pulse of 0.8mJ and 150 mbar (- -), showing the widening of harmonics with increasing pressure, as seen in [1]

Figure 4.9 shows the normalized statistical spectra generated from pump pulses of 0.8 mJ and 60 and 150 mbar, respectively. These data show that the harmonics become wider as the pressure is increased, an effect noted experimentally in [1]. At low gas pressures there is very little pulse breakup, and with the long 40 fs FWHM, the pump pulse spectrum remains relatively narrow, resulting in almost exclusively XUV frequencies at the harmonic frequencies of the carrier (800 nm). At higher pressures the increased nonlinearity leads to increased pulse breakup and more few cycle subpulses, resulting in a wider range of pump pulse frequencies, and given that each pump pulse frequency produces XUV of its own harmonic frequencies, this widens the HHG spectrum around each of the carrier (800 nm) frequency harmonics. This is a significant triumph for the statistical spectra as the extreme frequencies often seen in the full pump pulse are not fully considered here given that each subpulse is reduced to a simple Gaussian intensity profile. It is, however, implausibly difficult to compare this to the spectra explicitly

simulated through the semi-classical method, given that those spectra contain a lot of noise and very nontrivial pule shapes and hence, as seen in figures 4.3 and 4.6, without including the full radial pulse and post-capillary free space propagation, the intensity spikes which usually correspond to the harmonics are poorly defined.

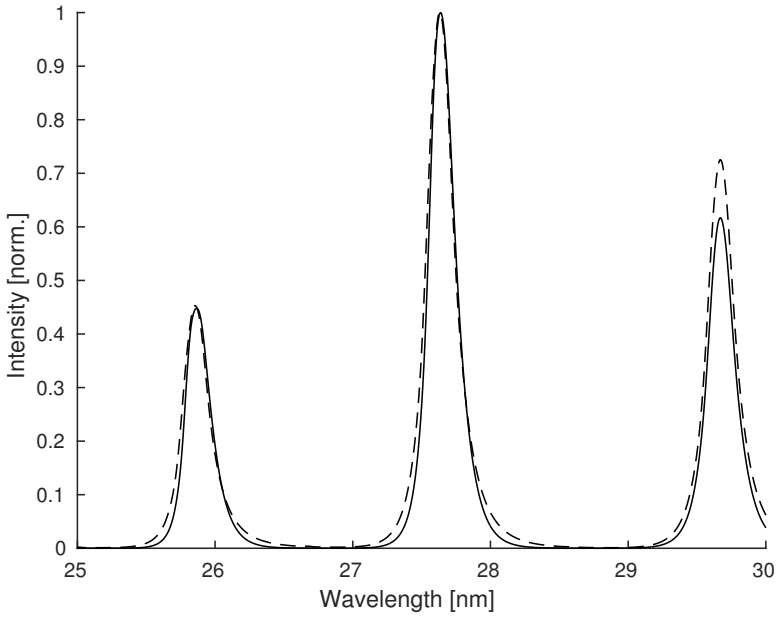

Figure 4.10: Plot showing the statistical spectra generated from a pump pulse of 1.1 mJ and 60 mbar (–), and from a pump pulse of 1.1mJ and 150 mbar (- -), showing the widening of harmonics with increasing pressure which supports the conclusions draw from figure 4.9

Figure 4.10 shows the normalised statistical spectra generated from pump pulses of 1.1 mJ energy and 60 and 150 mbar pressure, respectively. Although slightly less pronounced, these data support the conclusions drawn from figure 4.9, showing evidence of harmonics widening at increasing pressures although this behaviour is suppressed at this higher pulse energy. This is because in the prior case, the difference in nonlinearity between 60 and 150 mbar at 0.8 mJ is huge, whereas in the 1.1 mJ case, 60 mbar already represents a significant amount of nonlinearity and hence pulse breakup. Increasing the pressure to 150 mbar does increase the level of nonlinearity and hence pulse breakup, but given that the pulse is significantly fractured at lower pressures, this difference is much less noticeable and hence the resulting pump pulse spectrum widening and subsequent harmonic widening is suppressed.

Figure 4.11 shows a widening of the harmonics with fixed gas pressure and increasing pulse energy. This gives credence to the analysis of figure 4.9 which attributes widening harmonics to greater nonlinearity in the pump pulse resulting in more pulse breakup and hence a wider spectrum of pump pulse frequencies. The fixed pressure and varied pulse energy is simply a more extreme method of increasing nonlinearity in the system and hence it is unsurprising that widening between the 0.6 and 1.1 mJ cases is so pronounced.

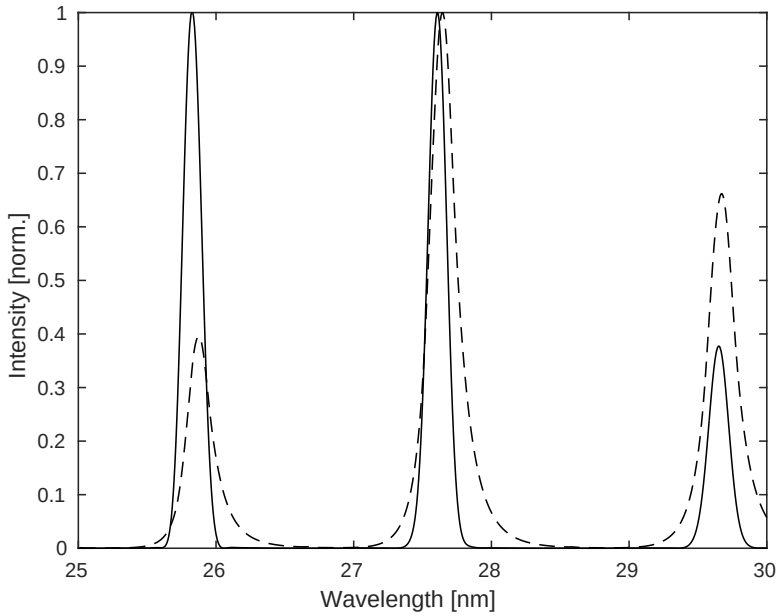

Figure 4.11: Plot showing the statistical spectra generated from a pump pulse of 100 mbar and 0.6 mJ (–), and from a pump pulse of 100 mbar and 1.1 mJ (- -), showing the widening of harmonics with increasing pulse energy, as seen in [1]

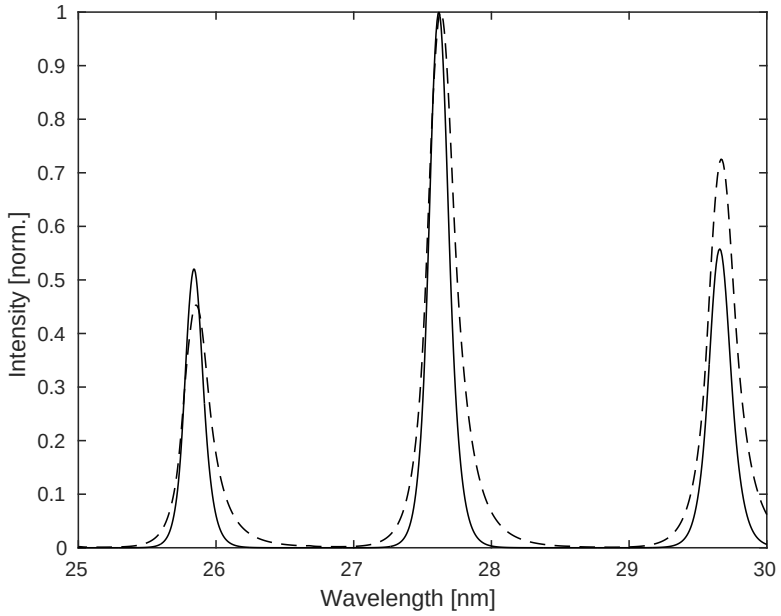

Figure 4.12: Plot showing the statistical spectra generated from a pump pulse of 150 mbar and 0.7 mJ (–), and from a pump pulse of 150 mbar and 1.1 mJ (- -), showing the widening of harmonics with increasing pulse energy.

Figure 4.12 shows the statistical spectra generated from pump pulses in 150 mbar with 0.7 and 1.1 mJ energy, respectively. It clearly shows the same widening of harmonics,

although again, as seen in the comparison of figures 4.9 and 4.10, the effect is less pronounced because the level of nonlinearirty is high in both cases and so there is a smaller relative difference in the number of subpulses between the two.

4.6 XUV Energy Buildup

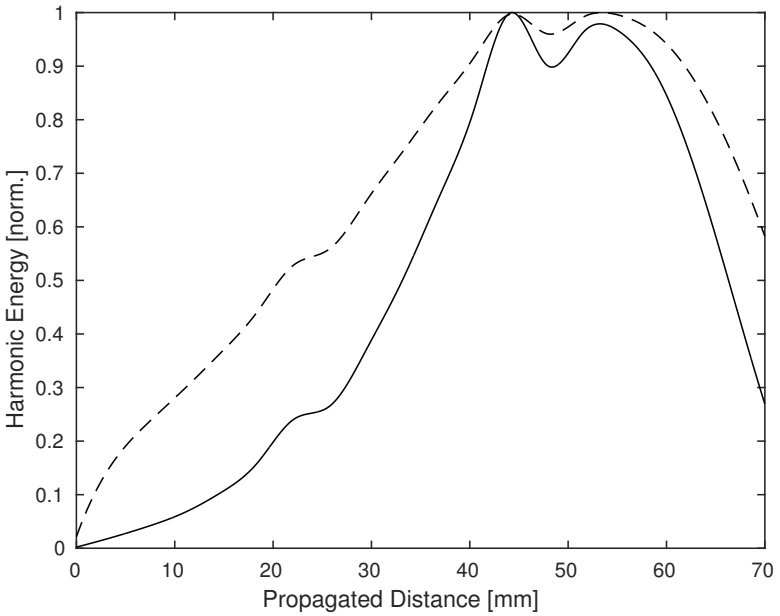

Figure 4.13: Plot showing the energy in the cumulative statistical spectrum at "standard parameters" for a range of different propagation lengths, for the coherently (–) and incoherently (- -) summed spectra. Note the peak at 45mm, coinciding with the optimum capillary length predicted by [2]

Figure 4.13 shows the energy of the coherent and incoherent statistical spectra at 0.8 mJ, 100 mbar, for a range of different propagation lengths. The behaviour of this quantity is determined by the quantity of XUV of a given wavelength generated relative to the absorption rate of argon for that wavelength, as given by figure 2.11. This implies that more intense subpulses, which generate more XUV in the 20-30 nm argon "window", will have a potentially positive effect on the growth of total harmonic energy, whereas low intensity subpulses will primarily generate in the 30-78nm region, where argon absorbs heavily, resulting in severely diminished XUV energy growth, or even potential XUV energy loss. This is seen particularly in the 30-40mm propagation region, around where the most intense peak of the propagation is found, as mentioned in section 3.6; here the energy in the generated XUV pulse grows significantly faster than at any other point in the propagation, primarily due to the large flux of 20-30 nm harmonics generated by the primary subpulse.

This result falls in agreement with the work of [2] and [?]3 who predict optimal XUV flux from a 45mm length of 150 μm diameter capillary. In the aforementioned papers only the peak pump pulse intensity is used to predict the optimal capillary length, ignoring all other subpulses and considering only pump pulse behaviour. Here we have reproduced the result by consideration of all subpulses and the XUV they would generate which indicates some validity in the way that total XUV flux is considered in this method.

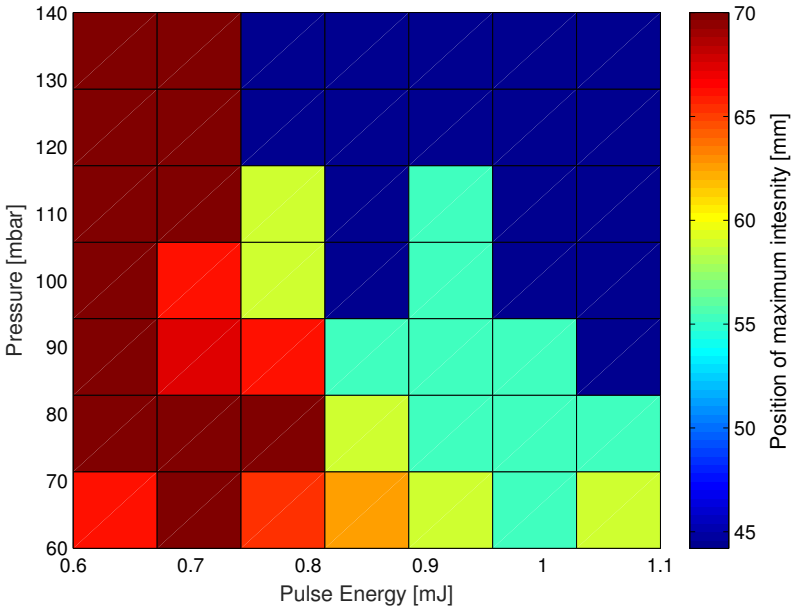

Figure 4.14: Plot showing the distance, in mm, along the capillary at which the coherently integrated spectra predict maximum XUV flux, as seen in figure 4.13 Note: for the $(U, p) \in \{(0.6714, 82.86), (0.6714, 94.2857), (0.7429, 60)\}$, a global optimization method is required for bivariate distribution fitting and hence these values are interpolated from the rest of the data.

Figure 4.14 shows the distance along the capillary at which the XUV flux is maximum, as predicted by the coherently integrated statistical spectra. It agrees with the 45 mm maximum for 0.8 mJ, 100 mbar, from [13] and figure 4.13, which is expected given that this is the beat length between the $LP_{0,1}$ and $LP_{0,2}$ modes, and for most significant levels of nonlinearity the $LP_{0,2}$ is strongly excited. By the same logic, the low energy propagation have extremely long build up lengths, which, given that most of their energy is contained within the $LP_{0,1}$ mode with little coupling into higher modes, resulting in an absorption-limited build up where the only limitation is that eventually enough of the pulse energy will be absorbed/dispersed by the gas to result in no significant XUV generation, although this distance is clearly longer than the 70 mm capillary considered. The shorter build up length seen predicted for 0.6 mJ 60 mbar seems to indicate that some effect is increasing the mode coupling at that point resulting in shorter build up distance, although this point has the lowest nonlinearity of any considered and almost all energy in the pump pulse is in the $LP_{0,1}$ mode, and so one would expect an extremely

long build up length. The most likely explanation for this prediction is that there is so little change in the pump pulse that there is a very sparse $\tilde{I}$ and $\tilde{T}$ distribution and hence the statistical method does not provide a strong prediction at this point. Overall, however, figure 4.14 agrees with intuitive and qualitative behaviours of the system and may serve as a useful prediction tool for future experiments.

Chapter 5

Summary

This thesis has introduced some useful and potentially important methodology for dealing with capillary-based HHG and other more nonlinear applications such as filamentation. The subpulse deconstruction allows for another way of analysing such nonlinear behaviour without relying on simple indicators such as pump pulse peak powers or total pump pulse widths, providing a more complete view of the pump pulse propagation and its implications for the generated XUV spectrum. Above this, the method provides a strong framework for analysing the overall behaviour of the pump pulse, giving qualitative data on the level of nonlinearity present in the system and the stability of the subpulse structure.

Following the introduction of the pump pulse deconstruction, the statistics of the subpulse ensemble were introduced, and with some normalisation and rescaling allowing analysis of the statistics of the whole subpulse ensemble, reducing the complexity and non-triviality of the pump pulse propagation to a few simple fitting constants and allowing easy comparison of different pump pulses.

Although the statistical spectra do not immediately provide the easy route to calculating HHG spectra directly from pump pulse characteristics as originally intended, they do not produce entirely dissimilar results and with some future inclusion of additional phase matching could provide an accurate approximation. Even though it does not exactly recreate the explicitly simulated spectra, the statistical spectra provide insight into the nature of HHG in capillaries, such as the complex phase profiles generated from the outer subpulses of the pump pulse, a region usually ignored in pump pulse analysis, and the way in which the interplay between this phase-matched harmonic growth and the absorption of the generating medium dictate the structure and flux of any generated XUV.

The statistical spectra also provide some predictions which hold true when compared to experimental and simulated data; for example, the widening of the harmonics for

increasing levels of nonlinearity seen in section 4.4 shows that the same fundamental behaviours are at work in the statistical system as in experiment and providing qualitative predictions for harmonic behaviours at different levels of nonlinearity. The statistical spectra also provide a rough guide to the scaling of the XUV flux for varying pulse energies although this is mostly just an implication of the strong recreation of the propagating harmonic flux as seen in figure 4.13 which accurately predicts the point along the capillary at which the generated XUV will have maximum energy, an invaluable prediction for the purpose of building capillary-based HHG systems which produce optimal flux.

The computational efficiency of the method, as discussed in section 4.1, makes the statistical spectra particularly apt for mass simulation, particularly for large parameter scans where using explicit semi-classical spectra could result in months of simulation time for even small scan sizes ($\sim$ 48 full semi-classical simulations compared to $\sim$ 2740 statistical simulations per month per cpu), and this huge increase in time efficiency and ability to simulate en masse could easily compensate for the loss of spectral accuracy seen in the statistical spectra.

Overall, the system produces many predictions and provides many insights into the nature of capillary-based HHG, and with some further development could produce a robust system for fast and effective estimation of generated XUV spectra for the purpose of optimisation and XUV source development.

Chapter 6

Future work

6.1 Phase

The most obvious potential continuation of the work in this thesis is the addition of phase information to the subpulse deconstruction and then to the final statistical spectrum calculation. The simplest method of implementing this would be by recording primary subpulse phases at the pulse deconstruction and using that phase to weight precalculated spectra in the statistical spectrum construction. The problem then arises that even in the semi-classical model the generated XUV depends non trivially on the phase of the pump pulse (see equation 2.10), and so ideally separate spectra should be precalculated for a fine grid of phases in addition to the intensity and width parameters already being considered. Unfortunately with the current method for precalculating and storing single-atom HHG spectra the data requirements would be huge, but it could be reduced through a variety of data compression and decimation methods.

The final consideration for improving the phase matching model of the statistical spectra is by considering intra-pulse subpulse interactions. This would involve including phase information for every contributing subpulse and hence would account for most of the phase matching-related effects seen in explicit simulations, particularly the off-harmonic components and fine harmonic envelope shape. Such a system would require extensive improvements in the computational efficiency of the generation, storage, and calling of the precalculated HHG spectra.

6.2 Off-axis effects

One of the major differences between the spectra explicitly simulated in this thesis and those observed in the lab is that those observed experimentally have smoother spectra with more clearly defined but wider harmonics. This is because of the averaging

that results from far-field propagation of a 3D field, and how this propagation brings similar wavelengths together resulting in a smoothed and spatially discrete spectrum of harmonics as opposed to the raw axial spectra seen in simulations. To include these propagation effects, the generation can be simulated on a radial grid and the result propagated into the far-field to simulate the travel distance to the detector inherent in experiment. This would, of course, dramatically increase the computational load off a single simulation, although it would improve the statistical method's ability to approximate experimental results.

The inclusion of off-axis effects also introduces the opportunity to consider non radially symmetric pump pulse coupling and the excitement of non radially symmetric capillary modes and the unique pump pulse and XUV pulse shapes which can arise from non symmetric pulses. It would also increase the method's ability to account for experimental inaccuracies and effects, some of which result in unique intensity growths and hence XUV spectra which are extremely difficult to model explicitly.

Appendix A

A.1 Coefficient Tableaux

Here are the coefficient tableaux for a and b from $n_{sub} \approx az^3+bz^2+1$, as well as $R^2(n_{sub})$ and the pump pulse peak intensity I_{peak}. Note: $U_0 = 0.8$mJ and $p_0 = 100$mbar.

A.1.1 $a(U,p)$ (figure 3.8) coefficients:

$$a(U,p) = \sum_{i=1}^{5}\sum_{j=1}^{i} c_{i,j}(U-U_0)^{i-j}(p-p_0)^{j-1} \text{ subpulses/mm}^3 \tag{A.1}$$

j						
5	-4.11e-5					
4	-1.45e-4	-3.91e-7				
3	-1.23e-4	-1.26e-6	2.21e-9			
2	-1.58e-4	-2.53e-6	5.06e-9	5.02e-11		
1	4.82e-4	-2.52e-6	1.04e-8	2.15e-11	-7.37e-13	
$c_{i,j}$	1	2	3	4	5	i

A.1.2 $b(U,p)$ (figure 3.9) coefficients:

$$B(U,p) = \sum_{i=1}^{5}\sum_{j=1}^{i} c_{i,j}(U-U_0)^{i-j}(p-p_0)^{j-1} \text{ subpulses/mm}^2 \tag{A.2}$$

j						
5	5.13e-3					
4	0.0161	4.36e-5				
3	2.51e-3	1.12e-4	-2.07e-7			
2	5.09e-3	1.14e-4	-5.76e-7	-2.82e-9		
1	-0.0215	1.48e-4	-5.66e-7	-7.83e-10	4.03e-11	
$c_{i,j}$	1	2	3	4	5	i

A.1.3 R^2 for $n_{sub}(z, U, p)$ coefficients:

$$R^2(U,p) = \sum_{i=1}^{5}\sum_{j=1}^{i} c_{i,j}(U-U_0)^{i-j}(p-p_0)^{j-1} \tag{A.3}$$

j						
5	0.941					
4	0.237	5.44e-4				
3	-2.13	-7.41e-3	-1.66e-5			
2	5.90	0.0155	4.19e-5	1.41e-7		
1	-6.05	-9.01e-3	5.80e-5	7.77e-8	-7.89e-10	
$c_{i,j}$	1	2	3	4	5	i

A.1.4 Pump-pulse peak intensity (figure 3.11) fit coefficients:

$$I_{peak}(U,p) = \sum_{i=1}^{5}\sum_{j=1}^{i} c_{i,j}(U-U_0)^{i-j}(p-p_0)^{j-1}\ \mathrm{W/cm^2} \tag{A.4}$$

j						
5	5.25e14					
4	6.56e14	-2.61e7				
3	-1.55e9	-1.25e8	7.91e6			
2	3.87e10	1.32e8	7.31e6	3.64e3		
1	-5.59e10	3.58e8	4.14e7	1.19e5	-751	
$c_{i,j}$	1	2	3	4	5	i

References

[1] S. L. Stebbings, E. T. F. Rogers, A. M. de Paula, M. Praeger, C. A. Froud, B. Mills, D. C. Hanna, J. J. Baumberg, W. S. Brocklesby, and J. G. Frey, "Molecular variation of capillary-produced soft x-ray high harmonics," *Journal of Physics B: Atomic, Molecular and Optical Physics*, vol. 41, p. 145602, July 2008.

[2] P. Anderson, P. Horak, J. Frey, and W. Brocklesby, "High-energy laser-pulse self-compression in short gas-filled fibers," *Physical Review A*, vol. 89, no. 1, p. 013819, 2014.

[3] T. Maiman, "Optical and microwave-optical experiments in ruby," *Physical Review Letters*, vol. 4, no. 11, p. 564, 1960.

[4] C. K. N. Patel, "Continuous-wave laser action on vibrational-rotational transitions of CO_2," *Physical Review*, vol. 136, no. 5A, p. A1187, 1964.

[5] P. F. Moulton, "Spectroscopic and laser characteristics of Ti:Al_2O_3," *Journal of the Optical Society of America B*, vol. 3, no. 1, p. 125, 1986.

[6] P. Franken, A. Hill, C. Peters, and G. Weinreich, "Generation of optical harmonics," *Physical Review Letters*, vol. 7, no. 4, p. 118, 1961.

[7] G. H. C. New and J. F. Ward, "Optical third-harmonic generation in gases," *Phys. Rev. Lett.*, vol. 19, p. 556, Sep 1967.

[8] N. H. Burnett, H. A. Baldis, M. C. Richardson, and G. D. Enright, "Harmonic generation in CO2 laser target interaction," *Applied Physics Letters*, vol. 31, no. 3, p. 172, 1977.

[9] R. W. Waynant and R. C. Elton, "Review of short wavelength laser research," *Proceedings of the IEEE*, vol. 64, no. 7, p. 1059, 1976.

[10] M. W. Zürch, *High-Resolution Extreme Ultraviolet Microscopy: Imaging of Artificial and Biological Specimens with Laser-Driven Ultrafast XUV Sources*. Springer, 2014.

[11] A. McPherson, G. Gibson, H. Jara, and U. Johann, "Studies of multiphoton production of vacuum-ultraviolet radiation in the rare gases," *Journal of the Optical Society of America B*, vol. 4, no. 4, p. 595, 1987.

[12] A. Rundquist, C. G. Durfee III, Z. Chang, C. Herne, S. Backus, M. N. Murnane, and H. C. Kapteyn, "Phase-Matched Generation of Coherent Soft X-rays," *Science*, vol. 280, p. 1412, May 1998.

[13] T. J. Butcher, P. N. Anderson, R. T. Chapman, P. Horak, J. G. Frey, and W. S. Brocklesby, "Bright extreme-ultraviolet high-order-harmonic radiation from optimized pulse compression in short hollow waveguides," *Physical Review A*, vol. 87, p. 043822, Apr. 2013.

[14] A. D. Parsons, R. T. Chapman, P. Baksh, B. Mills, S. Bajt, W. S. Brocklesby, and J. G. Frey, "Ultra-broadband support determination for extreme ultraviolet coherent diffractive imaging from a high harmonic source," *Journal of Optics*, vol. 15, p. 094009, Sept. 2013.

[15] B. Zhang, D. F. Gardner, M. D. Seaberg, E. R. Shanblatt, H. C. Kapteyn, M. M. Murnane, and D. E. Adams, "High contrast 3d imaging of surfaces near the wavelength limit using tabletop euv ptychography," *Ultramicroscopy*, vol. 158, p. 98, 2015.

[16] A. L. Cavalieri, N. Müller, T. Uphues, V. S. Yakovlev, A. Baltuska, B. Horvath, B. Schmidt, L. Blümel, R. Holzwarth, S. Hendel, M. Drescher, U. Kleineberg, P. M. Echenique, R. Kienberger, F. Krausz, and U. Heinzmann, "Attosecond spectroscopy in condensed matter.," *Nature*, vol. 449, p. 1029, Oct. 2007.

[17] M. B. Gaarde, J. L. Tate, and K. J. Schafer, "Macroscopic aspects of attosecond pulse generation," *Journal of Physics B: Atomic, Molecular and Optical Physics*, vol. 41, no. 13, p. 132001, 2008.

[18] G. Binnig, C. Quate, and C. Gerber, "Atomic force microscope," *Physical Review Letters*, vol. 56, no. 9, 1986.

[19] E. Ruska, *The Early Development of Electron Lenses and Electron Microscopy.* Microscopica Acta: Supplement, Hirzel, 1980.

[20] G. Binnig, H. Rohrer, C. Gerber, and E. Weibel, "Surface studies by scanning tunneling microscopy," *Physical Review Letters*, vol. 49, no. 1, p. 57, 1982.

[21] G. Meyer and N. M. Amer, "Novel optical approach to atomic force microscopy," *Applied Physics Letters*, vol. 53, no. 12, p. 10457, 1988.

[22] P. Hansma, V. Elings, O. Marti, C. Bracker, *et al.*, "Scanning tunneling microscopy and atomic force microscopy: application to biology and technology," *Science*, vol. 242, no. 4876, p. 209, 1988.

[23] C. J. Schwarz, Y. Kuznetsova, and S. R. J. Brueck, "Imaging interferometric microscopy.," *Optics Letters*, vol. 28, p. 1424, Aug. 2003.

[24] S. W. Hell, E. H. Stelzer, S. Lindek, and C. Cremer, "Confocal microscopy with an increased detection aperture: type-B 4Pi confocal microscopy.," *Optics Letters*, vol. 19, p. 222, Feb. 1994.

[25] E. Ash and G. Nicholls, "Super-resolution aperture scanning microscope," *Nature*, no. 237, p. 510, 1972.

[26] R. Kienberger and E. Goulielmakis, "Atomic transient recorder," *Nature*, vol. 427, no. 6977, p. 817, 2004.

[27] M. Chini, K. Zhao, and Z. Chang, "The generation, characterization and applications of broadband isolated attosecond pulses," *Nature Photonics*, vol. 8, no. 3, p. 178, 2014.

[28] R. Walker, "Progress with the DIAMOND light source project," *PAC*, no. 3, p. 232, 2003.

[29] J. Bozek, "AMO instrumentation for the LCLS X-ray FEL," *The European Physical Journal-Special Topics*, vol. 169, no. 1, 2009.

[30] Stanford University, "LCLS FAQ." https://portal.slac.stanford.edu/sites/lclscore_public/Lists/LCLS_FAQ/FAQ.aspx, 2014.

[31] D. Strickland and G. Mourou, "Compression of amplified chirped optical pulses," *Optics Communications*, vol. 56, no. 3, p. 219, 1985.

[32] J. L. Krause, K. J. Schafer, and K. C. Kulander, "Calculation of photoemission from atoms subject to intense laser fields," *Physical Review A*, vol. 45, no. 7, p. 4998, 1992.

[33] P. B. Corkum, "Plasma perspective on strong field multiphoton ionization," *Physical Review Letters*, vol. 71, no. 13, p. 1994, 1993.

[34] K. Schafer, B. Yang, L. DiMauro, and K. Kulander, "Above threshold ionization beyond the high harmonic cutoff," *Physical Review Letters*, vol. 70, no. 11, p. 1599, 1993.

[35] M. Lewenstein, P. Balcou, M. Y. Ivanov, A. Lhuillier, and P. B. Corkum, "Theory of high-harmonic generation by low-frequency laser fields," *Physical Review A*, vol. 49, no. 3, p. 2117, 1994.

[36] C. Durfee III, A. Rundquist, and S. Backus, "Phase matching of high-order harmonics in hollow waveguides," *Physical Review Letters*, vol. 83, no. 11, p. 2187, 1999.

[37] E. Marcatili and R. Schmeltzer, "Hollow metallic and dielectric waveguides for long distance optical transmission and lasers," *Bell System Technical Journal*, vol. 43, no. 4, p. 1783, 1964.

[38] C. Courtois, A. Couairon, B. Cros, J. R. Marques, and G. Matthieussent, "Propagation of intense ultrashort laser pulses in a plasma filled capillary tube: Simulations and experiments," *Physics of Plasmas*, vol. 8, no. 7, p. 3445, 2001.

[39] M. Kolesik and J. Moloney, "Nonlinear optical pulse propagation simulation: From Maxwell's to unidirectional equations," *Physical Review E*, vol. 70, no. 3, p. 036604, 2004.

[40] A. Gordon and F. X. Kärtner, "Quantitative modeling of single atom high harmonic generation," *Physical Review Letters*, vol. 95, no. 22, p. 223901, 2005.

[41] F. Poletti and P. Horak, "Description of ultrashort pulse propagation in multimode optical fibers," *Journal of the Optical Society of America B*, vol. 25, no. 10, p. 1645, 2008.

[42] E. T. F. Rogers, S. L. Stebbings, A. M. de Paula, C. A. Froud, M. Praeger, B. Mills, J. Grant-Jacob, W. S. Brocklesby, and J. G. Frey, "Spatiotemporal phase-matching in capillary high-harmonic generation," *Journal of the Optical Society of America B*, vol. 29, p. 806, Mar. 2012.

[43] V. S. Popov, "Tunnel and multiphoton ionization of atoms and ions in a strong laser field (Keldysh theory)," *Physics-Uspekhi*, vol. 47, p. 855, Sept. 2004.

[44] E. Priori, G. Cerullo, M. Nisoli, S. Stagira, S. De Silvestri, P. Villoresi, L. Poletto, P. Ceccherini, C. Altucci, R. Bruzzese, *et al.*, "Nonadiabatic three-dimensional model of high-order harmonic generation in the few-optical-cycle regime," *Physical Review A*, vol. 61, no. 6, p. 063801, 2000.

[45] H. Bethe and E. Salpeter, "Quantum mechanics of one-and two-electrons systems," *Handbuch der Physik*, vol. 35, p. 88, 1957.

[46] P. A. P. Moran, "Statistical Inference with Bivariate Gamma Distributions," *Biometrika*, vol. 56, p. 627, Dec. 1969.

[47] M. Abramowitz and I. Stegun, *Handbook of Mathematical Functions: With Formulas, Graphs, and Mathematical Tables*. Applied mathematics series, Dover Publications, 1964.